ESC-TR-2002-089

Quarterly Technical Report

Solid State Research

2003:1

Lincoln Laboratory

MASSACHUSETTS INSTITUTE OF TECHNOLOGY

LEXINGTON, MASSACHUSETTS

Prepared for the Department of the Air Force under Contract F19628-00-C-0002.

Approved for public release; distribution is unlimited.

20030710 024

This report is based on studies performed at Lincoln Laboratory, a center for research operated by Massachusetts Institute of Technology. The work was sponsored by the Department of the Air Force under Contract F19628-00-C-0002.

This report may be reproduced to satisfy needs of U.S. Government agencies.

The ESC Public Affairs Office has reviewed this report, and it is releasable to the National Technical Information Service, where it will be available to the general public, including foreign nationals.

This technical report has been reviewed and is approved for publication.

FOR THE COMMANDER

Gary Tutungian
Administrative Contracting Officer
Plans and Programs Directorate
Contracted Support Management

Non-Lincoln Recipients

PLEASE DO NOT RETURN

Permission is given to destroy this document when it is no longer needed.

Massachusetts Institute of Technology
Lincoln Laboratory

Solid State Research

Quarterly Technical Report
2003:1

1 November 2002 — 31 January 2003

Issued 3 July 2003

Approved for public release; distribution is unlimited.

Lexington Massachusetts

ABSTRACT

This report covers in detail the research work of the Solid State Division at Lincoln Laboratory for the period 1 November 2002 through 31 January 2003. The topics covered are Quantum Electronics, Electro-optical Materials and Devices, Submicrometer Technology, Biosensor and Molecular Technologies, Advanced Imaging Technology, Analog Device Technology, and Advanced Silicon Technology. Funding is provided by several DoD organizations—including the Air Force, Army, DARPA, MDA, Navy, NSA, and OSD—and also by the DOE, NASA, and NIST.

TABLE OF CONTENTS

	Abstract	iii
	List of Illustrations	vii
	List of Tables	x
	Introduction	xi
	Reports on Solid State Research	xiii
	Organization	xxiii
1.	QUANTUM ELECTRONICS	
	1.1 Short-Pulsed Nd:YAG/Cr^{4+}:YAG Passively *Q*-Switched Microchip Lasers	1
2.	ELECTRO-OPTICAL MATERIALS AND DEVICES	
	2.1 CO_2-Laser-Based RF Frequency Reference	5
3.	SUBMICROMETER TECHNOLOGY	
	3.1 Monolithic Detector Array Comprising More Than 1000 Aerial Image Sensing Elements	11
	3.2 Characterization of PAG Decomposition in Different Polymer Matrices at Advanced Lithographic Wavelengths	18
4.	BIOSENSOR AND MOLECULAR TECHNOLOGIES	
	4.1 EEL High-Energy-Density Biofuel Cell	27
5.	ADVANCED IMAGING TECHNOLOGY	
	5.1 Clock Tree Technique for Electrical Distribution of Signal Exposure Control for Focal Plane Arrays	33

6. ANALOG DEVICE TECHNOLOGY

6.1 Architecture for a Type-II Quantum Computer Coprocessor 37

7. ADVANCED SILICON TECHNOLOGY

7.1 Inherently Planar Fully Depleted Silicon-on-Insulator Isolation 43

LIST OF ILLUSTRATIONS

Figure No.		Page
1-1	Maximum repetition rate vs pulse width for lasers in Table 1-1.	3
2-1	Schematic of mixed-isotope dual-frequency CO_2 laser RF source.	6
2-2	Beat signal 2.153 285 GHz; vertical 10 dB/div, horizontal 100 Hz/div, resolution 10 Hz.	7
2-3	Beat frequency vs cavity length.	8
2-4	Beat frequency vs time for two different piezoelectric (PZT) bias points.	9
3-1	(a) Quantum yield and fluence dependence of Lincoln Laboratory buried-channel photodiode measured in photoconductive mode, and (b) normalized quantum yield of diode exposed to increasingly higher exposure doses. Both measurements were made at 193 nm.	12
3-2	Optical density spectrum for polysilicon aperture material used to cover the photodiodes. The polysilicon thickness is 120 nm.	14
3-3	Electron micrographs of sampling aperture fabricated onto the face of the active diodes: (a) 100-nm slit etched into 100 nm of polysilicon (after photoresist stripping), and (b) 200-nm slit etched into 200 nm of polysilicon (before photoresist stripping). In the final devices the polysilicon thickness is 120 nm and the bottom of the slit is comprised of the active photodiode.	15
3-4	Top-down schematic of the photoactive portion of the device.	17
3-5	Optical micrograph of in-process device corresponding to the schematic shown in Figure 3-4. Only the oxide encapsulation and the aluminum light shield must be added to complete the fabrication.	17
3-6	Measured (data points) and modeled (smooth curve) detector response to normal incidence polarized 193-nm radiation, as a function of the polarization orientation with respect to the slit. The slit was 200 nm wide and etched into 120-nm-thick poly-Si.	18
3-7	Chemical structures of di(phenylsulfonyl)diazomethane (DPSD), di(4-methylphenylsulfonyl)diazomethane (DMPSD), di(4-chlorophenylsulfonyl)diazomethane (DCPSD), and di(cyclohexylsulfonyl)diazomethane (DCHSD).	20

LIST OF ILLUSTRATIONS (Continued)

Figure No.		Page
3-8	Fourier transform infrared spectrum of 10% DPSD in Fox16 (FOX), showing loss of diazo absorbance at 2100 cm^{-1} with increasing exposure dose from back to front.	20
3-9	ProABC fit for 10% DPSD in FOX with 157-nm exposure.	21
3-10	ProABC fit for 10% DPSD in FOX with 193-nm exposure.	22
3-11	ProABC fit for 10% DPSD in FOX with 248-nm exposure.	22
3-12	Dill C values for all PAG and polymer combinations with 157-nm exposure.	23
3-13	Dill C values for all PAG and polymer combinations with 193-nm exposure.	24
3-14	Dill C values for all PAG and polymer combinations with 248-nm exposure.	24
4-1	HfaD targeting signals spliced to GFP gene.	27
4-2	Photographs of genetically engineered *Caulobacter* with targeted GFP, showing (a) DivJ signal localized to the stalk tip and (b) HfaD signal not localized to the stalk tip. Images were obtained with a 1000× fluorescent microscope.	28
4-3	Test of engineered bacteria with (a) fluorescence microscopy with SNARF-1 or other pH-sensitive dyes and (b) direct measurement of proton pumping.	29
4-4	Modeled performance of bacteria: (a) proton current density in relation to stalk length, and (b) temperature dependence.	29
4-5	Photographs showing attachment and maintenance of *Caulobacter* (a) on glass after 1 day, (b) on glass after 12 days, (c) on plastic after 1 day, and (d) on plastic after 12 days. Images were obtained with a 400× phase-contrast microscope with a charge-coupled device camera.	31
5-1	Example of H-tree clock distribution.	33
5-2	Signal fall time vs interconnect length $L2$ between repeaters for various fanouts M. Simulation done using a 0.18-μm bulk CMOS technology.	34
5-3	Unbalanced buffer/repeater; circuit numbers to the right signify width/length for the transistors.	34

LIST OF ILLUSTRATIONS (Continued)

Figure No.		Page
5-4	Pixel architecture showing support circuitry for distribution of the local and global clock.	35
6-1	Illustration of lattice-gas cellular automaton for the case of a square lattice with particle motion to nearest neighbors only. Alternating sequence of steps (a) through (d) is repeated many times for the entire lattice of nodes.	38
6-2	Illustration of architecture of a direct implementation of a Type-II quantum computer (T2QC). (a) Lattice of quantum nodes and the communication paths among them. Except for global control signals, each node communicates only with its neighbors (nearest neighbors only in this example). (b) Functional blocks needed in each node.	39
6-3	Architecture of quantum coprocessor for a T2QC. Each box labeled Q represents a complete quantum node containing a number of coherently coupled qubits (four for the example shown in the inset). The nodes are identical, and they are operated in parallel.	41
7-1	Scanning electron micrograph showing penetration of polysilicon gate into buried oxide (BOX) due to erosion of the BOX during processing. The wraparound of the silicon-on-insulator (SOI) reduces the edge threshold.	43
7-2	Drain current vs gate voltage for mesa-isolated n-FET and edgeless fully depleted SOI transistor. Premature turn-on of the edge of the mesa-isolated n-FET is evident when compared to the turn-on of an edgeless transistor. $L = 0.5\ \mu$m; $W = 8\ \mu$m; $V_{drain} = 0.05$ V.	44
7-3	Optical micrograph of underside of planar transistor after wafer bonding, active definition of the BOX and SOI, and probe pad etch. The probe pads are outside the field of view. Two tungsten plugs are exposed because of misalignment of active to polysilicon. The lower metal electrode was included for partially depleted device fabrication.	45
7-4	Cross section through transistor after isolation, showing the polysilion gate and the SOI and BOX stack. The sample was decorated to show the oxide-oxide bond.	45

LIST OF ILLUSTRATIONS (Continued)

Figure No.		Page
7-5	Transfer characteristics of planar (a) *n*-FET and (b) *p*-FET after isolation, passivation, and anneal. These devices received a second anneal of 20 min at 455°C. $L = 0.05\ \mu m$; $W = 20\ \mu m$.	46

LIST OF TABLES

Table No.		Page
1-1	Design and Operating Characteristics of Several Passively *Q*-Switched Microchip Lasers	1
3-1	Estimated Signal Levels from an Aperture-Covered Diode Coupled to a CCD	13
3-2	Optical Density Values (Base 10) for 120-nm-Thick Layers of Various Forms of Noncrystalline Silicon at the Three Main Excimer Laser Lithography Wavelengths	14
3-3	Process Flow for Monolithic Integration of the CCD, Photodiode, and Sampling Aperture	16

INTRODUCTION

1. QUANTUM ELECTRONICS

Passively Q-switched Nd:YAG/Cr^{4+}:YAG microchip lasers have demonstrated pulse widths <150 ps. For short-pulsed operation, the pulse width is dependent on the Nd concentration and is correlated with the maximum pulse rate achievable before thermal runaway.

2. ELECTRO-OPTICAL MATERIALS AND DEVICES

An unshielded free-running dual-frequency mixed-isotope 0.5-m CO_2 laser has produced a strong 2.153-GHz beat frequency with only 0.1-Hz/s drift in a noisy laboratory. A synthesizer-limited root-Allan variance $s_y < 6 \times 10^{-10}$ for $t = 2$ ms was obtained from phase-noise measurements.

3. SUBMICROMETER TECHNOLOGY

A monolithically integrated multielement photodiode array with 7749 discrete detectors has been fabricated, in which each sensing element is equipped with a sampling aperture to allow for aerial image measurements with high spatial precision in the focal plane of lithographic lenses. The high-speed analog output amplifier allows for complete 1107-element images to be obtained at the full repetition rate of lithographic lasers (2 KHz).

Fourier transform infrared spectroscopy was used to directly measure changes in the concentration of photoactive compound by isolating and measuring absorbance peaks unique to the photoactive species. These measurements were used to study the exposure kinetics of advanced photoresists and to provide valuable insights into the design of new resists.

4. BIOSENSOR AND MOLECULAR TECHNOLOGIES

Key principles for the EEL (Engineered Electrocyte Layers) biofuel cell have been demonstrated. Such cells should have up to 60× higher energy densities than batteries, could be easily refueled with any organic matter, and thus have the potential to revolutionize energy storage for a wide variety of applications.

5. ADVANCED IMAGING TECHNOLOGY

A clock tree technique has been demonstrated for electrical distribution of signal exposure control for focal plane arrays. An approach and implementation using an H-tree clock distribution network designed specifically for high-speed imaging in relatively large area arrays is described.

6. ANALOG DEVICE TECHNOLOGY

An architecture has been adopted for the development of a Type-II quantum computer (T2QC). The architecture is described, and its advantages over direct implementation of the standard architecture in a T2QC are enumerated.

7. ADVANCED SILICON TECHNOLOGY

A low-temperature oxide-oxide bond process has been developed that permits an alternate approach to fully depleted silicon-on-insulator (FDSOI) isolation by defining the SOI into islands after completion of conventional circuit fabrication. The SOI devices are isolated by an inherently planar technique that simplifies gate lithography and reduces field enhancement at island edges without the complexities of a shallow trench isolation process.

REPORTS ON SOLID STATE RESEARCH
1 NOVEMBER 2002 THROUGH 31 JANUARY 2003

PUBLICATIONS

Three-Dimensional Imaging Laser Radar with a Photon-Counting Avalanche Photodiode Array and Microchip Laser	M. A. Albota R. M. Heinrichs D. G. Kocher D. G. Fouche B. E. Player M. E. O'Brien B. F. Aull J. J. Zayhowski J. Mooney B. C. Willard R. R. Carlson	*Appl. Opt.* **41**, 7671 (2002)
Geiger-Mode Avalanche Photodiodes for Three-Dimensional Imaging	B. F. Aull A. H. Loomis D. J. Young R. M. Heinrichs B. J. Felton P. J. Daniels D. J. Landers	*Linc. Lab. J.* **13**, 335 (2002)
UV Cleaning of Contaminated 157-nm Reticles	T. M. Bloomstein V. Liberman M. Rothschild N. N. Efremow, Jr. D. E. Hardy S. T. Palmacci	*SPIE* **4346**, 669 (2001)

Thermal Conductivity of $AlAs_{0.07}Sb_{0.93}$ and $Al_{0.9}Ga_{0.1}As_{0.07}Sb_{0.93}$ Alloys and (AlAs)1/(AlSb)11 Digital-Alloy Superlattices	T. Borca-Tasciuc* D. W. Song* J. R. Meyer* I. Vurgaftman* M-J. Yang* B. Z. Nosho* L. J. Whitman* H. Lee* R. U. Martinelli* G. W. Turner M. J. Manfra	*J. Appl. Phys.* **92**, 4994 (2002)
Photospeed Considerations for Extreme Ultraviolet Lithography Resists	P. M. Dentinger* L. L. Hunter* D. J. O'Connell* S. Gunn* D. Goods* T. H. Fedynyshyn R. B. Goodman D. K. Astolfi	*J. Vac. Sci. Technol. B* **20**, 3962 (2002)
Morphology and Luminescence of Porous GaN Generated via Pt-Assisted Electroless Etching	D. J. Diaz* T. L. Williamson* I. Adesida* P. W. Bohn* R. J. Molnar	*J. Vac. Sci. Technol. B* **20**, 2375 (2002)
Reduction of Interfacial Recombination in GaInAsSb/GaSb Double Heterostructures	D. Donetsky* S. Anikeev* G. Belenky* S. Luryi* C. A. Wang G. Nichols*	*Appl. Phys. Lett.* **81**, 4769 (2002)

*Author not at Lincoln Laboratory.

Modeling of Acid Catalyzed Resists with Electron Beam Exposure	T. H. Fedynyshyn J. R. Gilman R. B. Goodman T. M. Lyszczarz S. J. Spector D. M. Lennon S. J. Deneault R. H. Bates	*SPIE* **4690**, 1126 (2002)
High Resolution Fluorocarbon Based Resist for 157-nm Lithography	T. H. Fedynyshyn W. A. Mowers R. R. Kunz R. F. Sinta M. Sworin R. B. Goodman	*SPIE* **4690**, 29 (2002)
Enhanced Resolution for Future Fabrication	M. Fritze C. K. Chen D. K. Astolfi D.-R. W. Yost J. A. Burns C.-L. Chen P. M. Gouker V. Suntharalingam P. W. Wyatt C. L. Keast	*IEEE Circuits Devices Mag.* **19**, 43 (2003)
Optical Imaging Properties of Dense Phase Shift Feature Patterns	M. Fritze B. M. Tyrrell R. D. Mallen B. D. Wheeler P. Rhyins* P. Martin*	*J. Vac. Sci. Technol. B* **20**, 2589 (2002)
Prospects for Photolithography at 121 nm	V. Liberman M. Rothschild P. G. Murphy S. T. Palmacci	*J. Vac. Sci. Technol. B* **20**, 2567 (2002)

*Author not at Lincoln Laboratory.

Electrical and Optical Properties of GaN/Al_2O_3 Interfaces	D. C. Look* R. L. Jones* X. L. Sun* R. J. Molnar J. E. Maslar* J. H. Han* S. S. Park* J. W. Ager* L. J. Brillson*	*J. Phys. Condens. Matter* **14**, 13337 (2002)
Resolution Enhancement of 157 nm Lithography by Liquid Immersion	M. Switkes M. Rothschild	*SPIE* **4691**, 459 (2002)
Investigation of the Physical and Practical Limits of Dense-Only Phase Shift Lithography for Circuit Feature Definition	B. M. Tyrrell M. Fritze D. K. Astolfi R. D. Mallen B. D. Wheeler P. Rhyins* P. Martin*	*J. Microlith. Microfab. Microsyst.* **1**, 243 (2002)
280 nm UV LEDs Grown on HVPE GaN Substrates	A. Yasan* R. McClintock* K. Mayes* S. R. Darvish* P. Kung* M. Razeghi* R. J. Molnar	*Opto-Electron. Rev.* **10**, 287 (2002)
Miniature, Pulsed Ti:Sapphire Laser System	J. J. Zayhowski A. L. Wilson, Jr.	*IEEE J. Quantum Electron.* **38**, 1449 (2002)

*Author not at Lincoln Laboratory.

PRESENTATIONS†

Periodically Poled $BaMgF_4$ for Ultraviolet Frequency Generation	S. C. Buchter* T. Y. Fan V. Liberman J. J. Zayhowski M. Rothschild E. J. Mason A. Cassanho* H. P. Jenssen* J. H. Burnett*	Lasers and Electro-Optics Society Annual Meeting, Glasgow, Scotland, 10-14 November 2002
AlGaAs/InGaAs 980-nm Slab-Coupled Semiconductor Lasers with Single-Spatial, Large-Diameter Mode	R. K. Huang J. P. Donnelly J. N. Walpole* L. J. Missaggia C. T. Harris R. J. Bailey J. J. Plant D. E. Mull W. D. Goodhue G. W. Turner	Lasers and Electro-Optics Society Annual Meeting, Glasgow, Scotland, 10-14 November 2002
Optical Down-Sampling of an X-Band 1-GHz-Bandwidth Nonlinear Chirp Signal	P. W. Juodawlkis J. J. Hargreaves R. D. Younger G. W. Titi J. C. Twichell	Lasers and Electro-Optics Society Annual Meeting, Glasgow, Scotland, 10-14 November 2002
Absorption Saturation Nonlinearity in InGaAs/InP p-i-n Photodiodes	P. W. Juodawlkis F. J. O'Donnell J. J. Hargreaves D. C. Oakley A. Napoleone S. H. Groves L. J. Mahoney K. M. Molvar	Lasers and Electro-Optics Society Annual Meeting, Glasgow, Scotland, 10-14 November 2002

*Author not at Lincoln Laboratory.

† Titles of presentations are listed for information only. No copies are available for distribution.

Development of Geiger-Mode Avalanche Photodiode Arrays for 1.06 μm	K. A. McIntosh J. P. Donnelly D. C. Oakley A. Napoleone S. D. Calawa L. J. Mahoney K. M. Molvar E. K. Duerr D. C. Shaver	Lasers and Electro-Optics Society Annual Meeting, Glasgow, Scotland, 10-14 November 2002
Accurate Spectral Analysis of Magneto-optical Permittivity of $Y_3F_5O_{12}$	G. F. Dionne G. A. Allen*	47th Conference on Magnetism and Magnetic Materials, Tampa, Florida, 11-15 November 2002
Optical Sampling for Analog-to-Digital Conversion	P. W. Juodawlkis J. J. Hargreaves R. D. Younger G. Betts* J. Twichell	Lincoln Laboratory Technical Seminar Series, University of California, Santa Barbara, California, 15 November 2002; Technical Seminar, University College London, United Kingdom, 15 November 2002
High-Frequency Nonlinear Surface Impedance of a Superconductor Strip	D. Agassi* D. Oates	2002 Fall Meeting of the Materials Research Society, Boston, Massachusetts, 2-6 December 2002
Spatial Variation of Transconductance in AlGaN/GaN Heterostructures Imaged by Scanning Gate Microscopy	J. W. P. Hsu* N. G. Weimann* M. J. Manfra K. W. West* D. V. Lang* R. J. Molnar	2002 Fall Meeting of the Materials Research Society, Boston, Massachusetts, 2-6 December 2002

*Author not at Lincoln Laboratory.

Growth of Thick InN by Molecular Beam Epitaxy	H. Lu* W. J. Schaff* L. F. Eastman* D. C. Look* J. Wu* W. Walukiewicz* R. J. Molnar	2002 Fall Meeting of the Materials Research Society, Boston, Massachusetts, 2-6 December 2002
Photonic-Crystal Distributed-Feedback Lasers	I. Vurgaftman* W. W. Bewley* C. L. Canedy* J. R. Lindle* C. S. Kim* J. R. Meyer* S. J. Spector D. M. Lennon G. W. Turner M. J. Manfra	2002 Fall Meeting of the Materials Research Society, Boston, Massachusetts, 2-6 December 2002
Canary B-Cell Sensor for Rapid, Sensitive Identification of Pathogens	J. D. Harper	Detection Technologies: The Next Generation in Identification and Analysis, Arlington, Virginia, 5-6 December 2002
A Compact SOI Model for 90/70 Nanometer Technology	P. Su* S. K. H. Fung* P. W. Wyatt H. Wan* A. Niknejad* M. Chan* C. Hu*	International Electron Devices Meeting, San Francisco, California, 9-11 December 2002
Integrated Photonic Devices for Time Delay Applications	S. J. Spector	Technical Seminar, Massachusetts Institute of Technology, Cambridge, Massachusetts, 18 December 2002

*Author not at Lincoln Laboratory.

Development of III-V Geiger-Mode Avalanche Photodiode Arrays for 1.06 μm	K. A. McIntosh J. P. Donnelly D. C. Oakley A. Napoleone S. D. Calawa	Semiconductor Detector Review, Anaheim, California, 8-9 January 2003
Immersion Lithography: Prospects and Challenges	M. Switkes R. R. Kunz M. Rothschild	International SEMATECH Workshop, San Francisco, California, 11-12 January 2003
Molecular Beam Epitaxy Growth of Advanced Antimonide-Based Alloys	G. W. Turner	Office of Naval Research Workshop on 6.1 Angstrom Semiconductors, Padre Island, Texas, 12-16 January 2003
High-Performance CCD Imagers for Low-Light-Level Applications	B. B. Kosicki	Lincoln Laboratory Technical Seminar Series, Massachusetts Institute of Technology, Cambridge, Massachusetts, 14 January 2003
High-Fill-Factor, Burst-Rate Charge-Coupled Device	R. K. Reich D. M. O'Mara D. J. Young A. H. Loomis	Lincoln Laboratory Technical Seminar Series, Massachusetts Institute of Technology, Cambridge, Massachusetts, 14 January 2003
High-Speed, Electronically Shuttered Solid-State Imager Technology	R. K. Reich D. M. Rathman	Lincoln Laboratory Technical Seminar Series, Massachusetts Institute of Technology, Cambridge, Massachusetts, 14 January 2003

Technology to Extend Optical Lithography to the End of Moore's Law	R. R. Kunz	Technical Seminar, IBM T. J. Watson Research Center, Yorkstown, New York, 24 January 2003

ORGANIZATION

SOLID STATE DIVISION

D. C. Shaver, Head
R. W. Ralston, Associate Head
N. L. DeMeo, Jr., Assistant
Z. J. Lemnios, Senior Staff
K. J. Challberg, Administrative Staff
J. D. Pendergast, Administrative Staff

SUBMICROMETER TECHNOLOGY

M. Rothschild, Leader
T. M. Lyszczarz, Assistant Leader
T. H. Fedynyshyn, Senior Staff
R. R. Kunz, Senior Staff

Astolfi, D. K.
Bloomstein, T. M.
Cann, S. G.
Creel, C. R.
DiNatale, W. F.
Efremow, N. N., Jr.
Geis, M. W.
Goodman, R. B.
Krohn, K. E.
Leibowitz, F. L.
Lennon, D. M.
Liberman, V.
Palmacci, S. T.
Pottebaum, I. S.
Sedlacek, J. H. C.
Spector, S. J.
Stallman, J. B.
Switkes, M.
Yoon, J. U.

QUANTUM ELECTRONICS

A. Sanchez-Rubio, Leader
T. Y. Fan, Assistant Leader
T. H. Jeys, Senior Staff
J. J. Zayhowski, Senior Staff

Aggarwal, R. L.
Augst, S. J.
Daneu, J. L.
Daneu, V.
Desmarais, L.
Goyal, A. K.
Herzog, W. D.
Hybl, J. D.
Le, X. T.
Lynch, E. J.
O'Brien, P. W.
Ochoa, J. R.
Ripin, D. J.

ELECTRO-OPTICAL MATERIALS AND DEVICES

J. C. Twichell, Leader
G. W. Turner, Assistant Leader
D. L. Spears, Senior Staff
C. A. Wang, Senior Staff
R. C. Williamson, Senior Staff

Bailey, R. J.
Calawa, D. R.
Calawa, S. D.
Connors, M. K.
Donnelly, J. P.
Goodhue, W. D.
Groves, S. H.
Hargreaves, J. J.
Harman, T. C.
Harris, C. T.
Huang, R. K.
Juodawlkis, P. W.
LaForge, B. E.
Liau, Z. L.
Mahoney, L. J.
Manfra, M. J.
McIntosh, K. A.
Missaggia, L. J.
Molnar, R. J.
Mull, D. E.
Napoleone, A.
Nitishin, P. M.
Oakley, D. C.
O'Donnell, F. J.
Plant, J. J.
Shiau, D. A.
Taylor, P. J.
Younger, R. D.

BIOSENSOR AND MOLECULAR TECHNOLOGIES

M. A. Hollis, Leader
T. H. Rider, Senior Staff

Blanchard, D. J.
Cabrera, C. R.
Graves, C. A.
Harper, J. D.
Lakdawala, S.
Mathews, R. H.
Nargi, F. E.
Parameswaran, L.
Petrovick, M. S.
Postema-Zook, C. E.
Schmidt, T. L.
Schwoebel, E. D.

ANALOG DEVICE TECHNOLOGY

M. A. Gouker, Leader
L. M. Johnson, Assistant Leader
A. C. Anderson, Senior Staff

Berggren, K. K.
Bolkhovsky, V.
Fitch, G. L.
Lyons, W. G.
Macedo, E. M., Jr.
Murphy, P. G.
Oates, D. E.
Sage, J. P.
Santiago, D. D.
Seaver, M. M.
Slattery, R. L.
Weir, T. J.

ADVANCED IMAGING TECHNOLOGY

B. B. Kosicki, Leader
R. K. Reich, Assistant Leader
B. E. Burke, Senior Staff

Aull, B. F.
Ciampi, J. S.
Cooper, M. J.
Craig, D. M.
Daniels, P. J.
Doherty, C. L., Jr.
Dolat, V. S.
Felton, B. J.
Gregory, J. A.
Johnson, K. F.
Lind, T. A.
Loomis, A. H.
Mallen, R. D.
McGonagle, W. H.
O'Mara, D. M.
Osgood, R. M.
Percival, K. A.
Rathman, D. D.
Rose, M. K.
Stern, A.
Young, D. J.

ADVANCED SILICON TECHNOLOGY

C. L. Keast, Leader
V. Suntharalingam, Assistant Leader
P. W. Wyatt, Senior Staff

Austin, E. E.
Berger, R.
Bozler, C. O.
Brunelle, M. R.
Burns, J. A.
Chen, C. K.
Chen, C. L.
D'Onofrio, R. P.
Fritze, M.
Gouker, P. M.
Healey, R. E.
Hu, W.
Knecht, J. M.
Lui, N. S.
Muldavin, J. B.
Newcomb, K. L.
Rabe, S.
Soares, A. M.
Travis, L.
Tyrrell, B. M.
Warner, K.
Wheeler, B. D.
Yost, D.-R.
Young, G. R.

1. QUANTUM ELECTRONICS

1.1 SHORT-PULSED Nd:YAG/Cr^{4+}:YAG PASSIVELY *Q*-SWITCHED MICROCHIP LASERS

Passively *Q*-switched microchip lasers based on a Nd:YAG gain medium and a Cr^{4+}:YAG saturable absorber have found numerous applications, and several designs have been reported in the literature [1]. For applications in high-resolution ranging and imaging, it is desirable to have lasers that produce short pulses at high repetition rates. Here, we report the shortest pulses obtained from a Nd:YAG/Cr^{4+}:YAG passively *Q*-switched laser. For short-pulsed operation, the pulse width is dependent on Nd concentration and is correlated with the maximum pulse rate achievable.

Table 1-1 summarizes the characteristics of several recently developed lasers. The cavity design is specified by the lengths of the undoped-YAG pump-side endcap l_{ic}, the Nd:YAG gain medium l_{Nd}, the Cr^{4+} saturable absorber l_{Cr}, and the undoped-YAG output-side endcap l_{oc}, all in millimeters, followed by the reflectivity R of the output coupler in percent. The transmission of the output mirrors was chosen to be

TABLE 1-1

Design and Operating Characteristics of Several Passively *Q*-Switched Microchip Lasers

	Cavity Design $l_{ic}/l_{Nd}/l_{Cr}/l_{oc}$–$R$ (mm-%)	Cr^{4+} Fill Factor F	Pulse Width t_w (ps)	Pulse Energy E (μJ)	Maximum Repetition Rate R_{max} (kHz)
SPMCL-0	1.0/3.0/1.5/1.0 -40	0.23	550	65	20
SPMCL-1	0.5/1.0/1.5/0.5 -40	0.43	308	36	5
SPMCL-2	0.5/1.5/1.5/0.5 -40	0.38	320	42	10
SPMCL-3	0.5/1.0/1.0/0.5 -55	0.33	405	25	16
SPMCL-4	–/1.0/1.5/– -40	0.60	248	26	5
SPMCL-5	–/1.5/1.5/– -40	0.50	221	37	4
SPMCL-6	–/1.0/1.0/– -55	0.50	260	22	5

approximately equal to the single-pass loss of the saturable absorber, to minimize the output pulse width of the laser. The Nd concentration is 1.4 wt%; the absorption coefficient α_{Cr} of the Cr^{4+} is ~6 cm^{-1} at 1064 nm.

The Cr^{4+} fill factor F is defined by $F = (\alpha_{Cr}/6\ cm^{-1})l_{Cr}/(l_{ic} + l_{Nd} + l_{Cr} + l_{oc})$. The minimum pulse width t_w obtainable with an ideal saturable absorber would be $55/F$ ps. For Cr^{4+}:YAG the pulse width is given by $\eta \times 55/F$ ps, where $1.1 < \eta < 2.5$. The smallest value of η is consistent with the ratio of the gain cross section of Nd^{3+} and the absorption cross section of Cr^{4+}. Larger values are typical of short-pulsed devices and are attributed to bleaching of the saturable absorber by the diode pump light. This effect is greatest when transmitted pump light is nearly focused in the Cr^{4+}:YAG (short Nd:YAG section) and when pumping is sufficiently intense to bleach the Nd:YAG. Both are important for short-pulsed lasers. The net effect is minimized with highly doped Nd:YAG.

The lasers listed in Table 1-1 were pulse pumped with high-brightness fiber-coupled diode laser arrays. The output of the pump fiber (200-μm core diameter, 0.22 NA) was focused into the microchip laser with an aspheric doublet, with a nominal magnification of 0.5. The actual magnification was fixed by adjusting the position of the lens to optimize the performance of the laser. Pump durations, electronically terminated by the firing of the microchip laser, varied between 25 and 70 μs, with a peak pump power of 20 W. The microchip lasers had a 2 × 2-mm cross section, and were heatsunk on the top and bottom.

The output pulse widths and energies of the microchip lasers, listed in Table 1-1, were recorded at 500 Hz, with the pump focusing optimized for minimum threshold (shortest pump duration). Pulse widths are dependent on pump focusing and often decrease with increasing repetition rate. SPMCL-6 had a pulse width as short as 169 ps at 500 Hz when the pump light was focused near the input facet of the laser (minimum threshold occurs when the pump light is focused further into the laser); SPMCL-5 had a 148-ps pulse width at 4 kHz when the pump focusing was optimized for minimum threshold at 500 Hz. Pulse energies also depend on pump focusing, since changes in pump focusing affect the diameter of the oscillating mode, while the threshold of a passively Q-switched laser is dependent on the intensity of light incident on the saturable absorber.

The pump-pulse duration of the lasers decreased or remained nearly constant as the pulse rate was increased from 500 Hz to the maximum repetition rate R_{max}. At R_{max}, a ~1% increase in the pulse rate resulted in thermal runaway, and the pump duration increased rapidly. For several of the lasers tested, thermal fracture occurred following thermal runaway, as the pump-pulse duty cycle approached 100%. To prevent thermal fracture, the maximum pump duty cycle was electronically limited for the remainder of the tests. For a given microchip laser, pump diode, and pump focusing, the value of R_{max} was extremely repeatable. It had ~30% scatter for different microchip lasers of the same design, when different pump diodes were used, or when the pump light was focused differently. The maximum R_{max} was achieved when the pump focusing was optimized for minimum threshold.

The maximum repetition rate is correlated with the Cr^{4+} fill factor and, therefore, the pulse width, as shown in Figure 1-1. As the Cr^{4+} fill factor increases, the fraction of the cavity filled with Nd:YAG decreases, and the Nd:YAG must be more highly inverted to reach threshold. More heat is deposited per

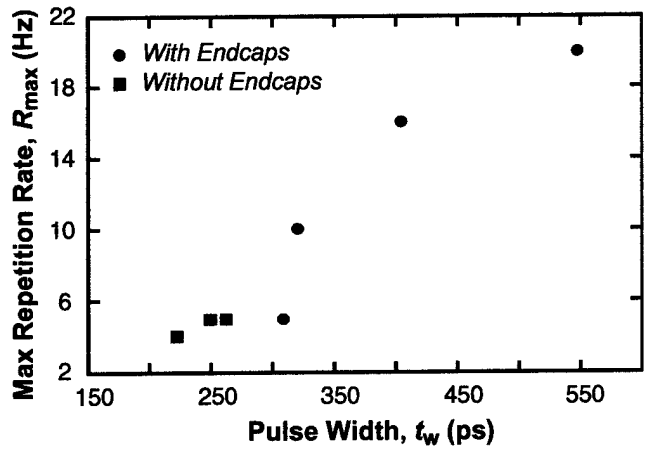

Figure 1-1. Maximum repetition rate vs pulse width for lasers in Table 1-1.

unit length of active material. As the Nd:YAG heats up, the gain cross section decreases, requiring even greater inversions. This and related effects result in positive feedback, leading to a well-defined threshold for thermal runaway. While there are design approaches that can reduce these effects, they have limitations and there is an inherent trade-off between the pulse width and the maximum repetition rate in this material system.

J. J. Zayhowski
A. L. Wilson

REFERENCES

1. J. J. Zayhowski, *Rev. Laser Eng.* **26**, 841 (1998).

2. ELECTRO-OPTICAL MATERIALS AND DEVICES

2.1 CO_2-LASER-BASED RF FREQUENCY REFERENCE

A dual-frequency CO_2 laser can generate RF reference frequencies that may offer significantly lower phase noise than present state-of-the-art oscillators. Based on the fundamental argument that the Schawlow-Townes linewidth sets the phase noise of any oscillator, the CO_2-laser-based RF source should be among the best oscillators possible because of its inherently high power output and cold-cavity Q.

Our approach, first explored by Freed more than 25 years ago [1],[2], consists of a CO_2 laser that uses two different isotopes of C and/or O and oscillates at two optical frequencies in a single very high Q optical cavity. The output is mixed on a wideband photomixer to produce RF power at the difference frequency. A CO_2 laser uses the vibrationally excited states of the gas, so different isotopes have different rotational-vibrational frequencies. For any one isotope, there are many, closely spaced rotational-vibrational lines with gain. Standard $^{16}O^{12}C^{16}O$ (abbreviated 626) will lase from 9.6 to 11 μm (or 31–27 THz) just in the four regular bands, each with a series of lines 30–60 GHz apart. Different isotopes will lase in mostly overlapping spectral regions. Closely spaced pairs of lines can be found with line-center frequency differences ranging from a few megahertz to tens of gigahertz. If the gains are sufficiently strong and similar, generally both lines will lase simultaneously in a two-isotope laser.

In the initial phase of the present effort, a CO_2 gas containing a 50/50 mix of the ^{16}O and ^{18}O isotopes (producing the 626, 828, and 628 molecules) and a 1.5-m grating-coupled laser [3] were used. Depending upon the pair of laser lines tuned in by the grating, RF beats at 0.89, 1.68, 2.13, 2.67, and 3.23 GHz were observed. The 1.5-m laser did not have sufficient long-term stability to enable phase-noise measurements. Allan variance measurements were carried out on the 890-MHz beat, from the 626 I-P(12) and 628 I-P(19) lines. The data, e.g., $s_y < 10^{-8}$ for $t = 0.1$ ms, indicated that for short time intervals (<0.2 ms) the laser beat was more stable than the 890-MHz signal from an HP8662 synthesizer, which uses a high-quality quartz reference oscillator. This was the same result as that obtained in 1979 with a more complex two-discharge-tube, 1.5-m grating-coupled laser [2]. However, in a grating-controlled laser the two lasing transitions do not in general have exactly the same optical cavity, which is a central premise for the expected high stability of the RF beat.

Free-running 0.5-m two-mirror CO_2 lasers [3],[4] have shown excellent short-term stability ($s_y \sim 10^{-13}$ for $t = 0.01$ s) at ~28 THz, far better than that for grating-coupled lasers. Indeed, radar returns from orbiting satellites were used to get long enough path lengths to simply bound the linewidth of these 0.5-m CO_2 lasers to <1 mHz. Our experimental setup is quite simple and shown schematically in Figure 2-1. CaF_2 plates were used to attenuate the output so that <0.2 mW was incident upon the 77-K HgCdTe photodiode photomixer [5]. The photomixer and optics were tilted to minimize feedback.

Detailed calculations indicate that a simple two-mirror laser could operate simultaneously at two frequencies if two strong gain lines are chosen and the output mirror has a very high reflectivity >96%. In

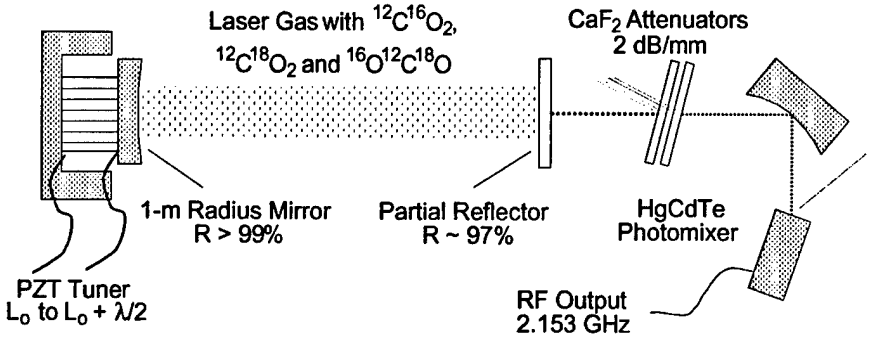

Figure 2-1. Schematic of mixed-isotope dual-frequency CO_2 laser RF source.

addition, the laser-cavity length must be such that the free spectral range is several times the linewidth and that both lines can simultaneously operate very near line center. In preliminary work with these 0.5-m lasers, we found a means of determining the precise cavity length. In tuning the length with the piezoelectric (PZT), the sequence in which the approximately 12 laser lines appear can be used to determine the precise cavity length, because the line-center frequencies are known to better than one part in 10^9 [6]. Here, the optical cavity length L_o ($V_{PZT} = 0$) was initially 478,112.5 ± 5.3 μm. With this information the desired length can be realized by simply inserting a precision shim under the flat mirror holder.

The goal of this work is to obtain an RF beat signal that has a stability similar to that of the laser lines, i.e., $s_y \sim 10^{-13}$ for $t \sim 0.01$ s. However in the 0.5-m lasers, the length of the gain region is only about 1/5 that of the 1.5-m lasers, so the gain is low. Lasing on the desired lines was achieved by (1) installing higher-reflectivity mirrors that suppress unwanted lines, (2) adjusting the laser gas mixture, and (3) cooling the discharge tube to 5°C. With an I-P branch selective, 97% reflectivity output mirror and a gas mixture containing about 61% ^{18}O, lasing on the I-R, II-P, and II-R lines was suppressed and dual-wavelength operation on the 626 I-P(18) and 628 I-P(25) lines was achieved with a total output power of ~150 mW. The strongest line in the 626 I-P branch is the I-P(20) line, whereas in the 628 I-P branch, it appears to be the I-P(23) line, so there are only about four lines with higher gain that need to be avoided by judicious choice of cavity length. With a total incident laser power of ~0.15 mW, the RF power from the photomixer was about –40 dBm. From these power levels we concluded that the power ratio of two laser lines was within 0.5 dB of unity. Figure 2-2 shows a typical RF beat signal. The beat frequency had –25-dB sidebands at 120 Hz, presumably a result of power supply ripple.

Gain pulling was found to dominate the stability of the 2.153-GHz beat. Although gain pulling has only a small effect on the two 28-THz laser frequencies, these effects do not cancel out on the 2-GHz beat

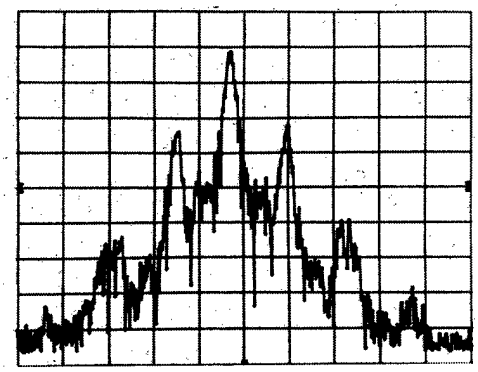

Figure 2-2. Beat signal 2.153 285 GHz; vertical 10 dB/div, horizontal 100 Hz/div, resolution 10 Hz.

frequency to the same high degree as cold-cavity tuning. Cancellation of gain-pulling effects requires (1) operating both lines at line center, which is only possible if the two line frequencies differ precisely by an integer number of cavity mode spacings, an unlikely situation; (2) both lines to have exactly the same Doppler and pressure broadened linewidth, which is not possible with different isotopes; and (3) the gains (losses) are identical for both lines. Figure 2-3 shows the measured and calculated variation of the beat frequency with cavity length. Very good agreement was found between the measured and calculated length dependence, which is quite different from that expected for cold-cavity tuning. To get this agreement, we assumed a 1-MHz difference in the pressure shift (a total gas pressure of 12.5 Torr was used) between the 626 and 628 molecules [7]. In our current laser, gain pulling at line center (peak output power) caused the beat frequency change with cavity length df/dL to be ~6 times larger than the –4.4 Hz/nm for cold-cavity tuning ($df/dL = f/L$). However, about 8 MHz from line center, df/dL goes to zero, a very desirable operating point. Further calculations indicate that by adjusting the cavity length and the loss (saturated gain) to match the 2.2% difference in linewidths, this $df/dL = 0$ point can be moved to line center.

As shown in Figure 2-4, when operating near the power peak, the measured drift was ~1 Hz/s, whereas operating near the $df/dL = 0$ point, the drift was as low as 0.1 Hz/s ($1/f\ df/dt = 5 \times 10^{-11}$/s). This result was achieved in a noisy room without an acoustic enclosure and typical (±2°C) laboratory temperature control. For the first time, phase-noise measurements were possible. Initial phase-noise measurements were done near line center and showed –122 dBc/Hz for frequency offsets from 5×10^3 to 5×10^7 Hz. From these data for $t = 2$ ms, we obtained $s_y = 6 \times 10^{-10}$, which was limited by reference oscillator noise. We expect considerably better results soon with modest improvements in temperature control and acoustic isolation and reduction in power supply noise.

D. L. Spears
J. J. Hargreaves
J. C. Twichell
C. Freed
J. G. Grimm

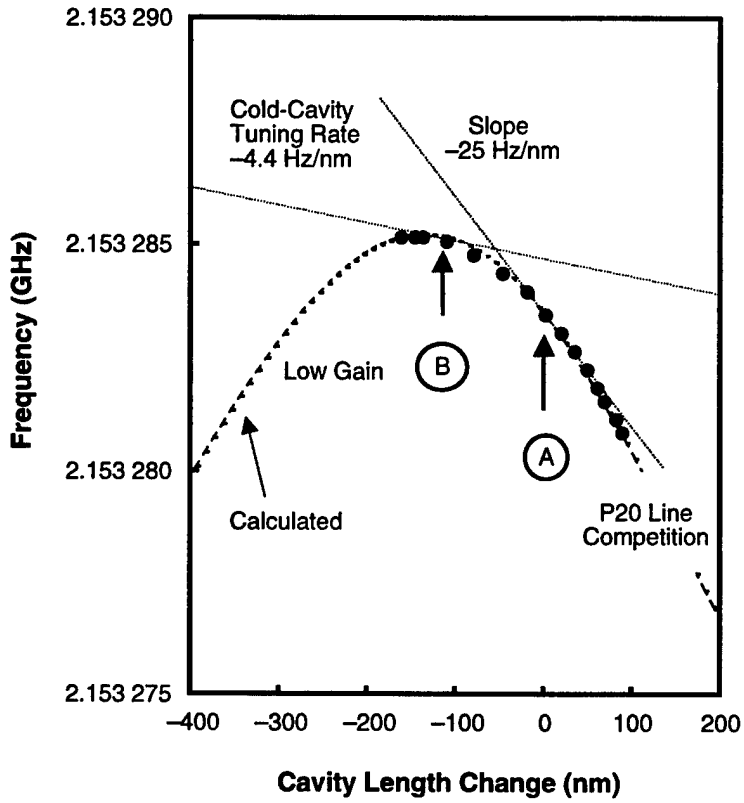

Figure 2-3. Beat frequency vs cavity length.

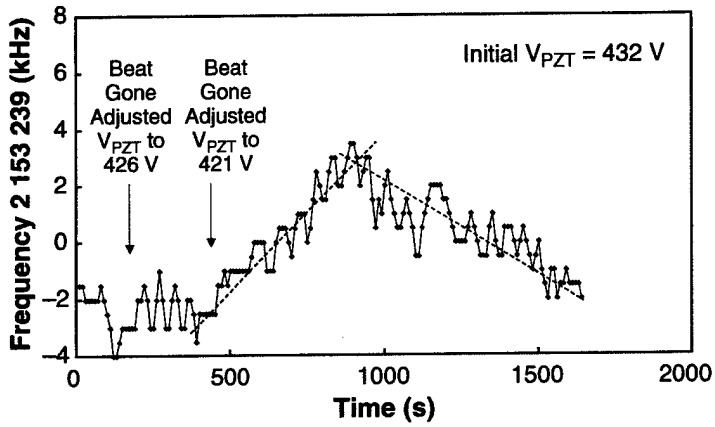

Figure 2-4. Beat frequency vs time for two different piezoelectric (PZT) bias points.

REFERENCES

1. C. Freed, *Proceedings of the 31st Annual Symposium on Frequency Control* (The Command, Washington, DC, 1977).

2. C. Freed, *Proceedings of the International Conference on Lasers '80* (STS Press, McLean, VA, 1981).

3. C. Freed, *Linc. Lab. J.* **3**, 479 (1990).

4. C. Freed, R. S. Eng, and C. L. Summers, *Proceedings of the International Conference on Lasers '93,* (STS Press, McLean, VA, 1994).

5. D. L. Spears, *Proc. SPIE* **300**, 174 (1980).

6. L. C. Bradley, K. L. SooHoo, and C. Freed, *IEEE J. Quantum Electron.* **QE-22**, 234 (1986).

7. K. L. SooHoo, C. Freed, J. E. Thomas, and H. A. Haus, *IEEE J. Quantum Electron.* **QE-21**, 1159 (1985).

3. SUBMICROMETER TECHNOLOGY

3.1 MONOLITHIC DETECTOR ARRAY COMPRISING MORE THAN 1000 AERIAL IMAGE SENSING ELEMENTS

Current trends in optical lithography are driving the minimum critical dimensions ever closer to the diffraction limit of the imaging optics. In order to meet this challenge, lithographers are finding it increasingly important to both quantify and monitor the residual aberrations in their lithography tools. However, once the tools are placed in the field these aberration measurements often require specialized masks and/or illumination schemes followed by off-line metrology of the resultant wafers [1]–[5].

We have undertaken the development of an electronic replacement for the photoresist-based recording medium used in these aberration measurements that will provide a fully closed-loop aberration measurement capability. The device consists of many (>1000) active sensing elements at or near the minimum critical dimension (100–200 nm), monolithically integrated onto a photodiode array equipped with an interline transfer charge-coupled device (CCD) for data readout through a high-speed (>1 MHz) analog output amplifier. This enables pulse-by-pulse full-field aerial image sampling at the full frequency of the lithographic laser source. There are several critical aspects to producing such a device, and a brief description of each will be provided.

Photodiodes designed for operation in the deep- to vacuum-ultraviolet (DUV-VUV) range (150–300 nm) have been commercially available for some time, and much is known about their operation. The design used in this study was based on the more radiation-hard *n*-on-*p* silicon photodiode [6] with the active surface passivated with a nitride-enhanced silicon dioxide [7],[8]. However, our need to integrate a monolithic stand-alone diode to an adjacent CCD added additional design constraints to ensure both process and performance compatibility with the CCD. For these reasons, we elected to use a buried-channel device with the *n-p* junction ~200 nm below the surface. This is in contrast to the ultra-shallow-channel devices usually selected for DUV-VUV applications to better accommodate the shallow photon penetration depth (as short as ~10 nm at 157 nm) [9]. Tests of stand-alone test diodes measured in the photoconductive mode indicated quantum efficiencies of ~0.1 for our buried-channel design, shown in Figure 3-1(a), compared to reported values of slightly greater than one for the shallow junction design. Reductions in quantum efficiency due to our buried-channel design were partially mitigated when integrated with the CCD arrays by tailoring a graded dopant profile in the active region to generate an electric field gradient to enhance charge migration toward the transfer gate and CCD. Given these values of quantum efficiency, we can estimate the signal levels expected for typical conditions. These results are shown in Table 3-1.

Further tests to investigate the diode's radiation durability indicated that the stability of these devices exceeds that measured for the best commercially available devices, with a loss in quantum efficiency of only ~25% after a 6000 J/cm^2 exposure at 193 nm, as seen in Figure 3-1(b). This dose is the equivalent of

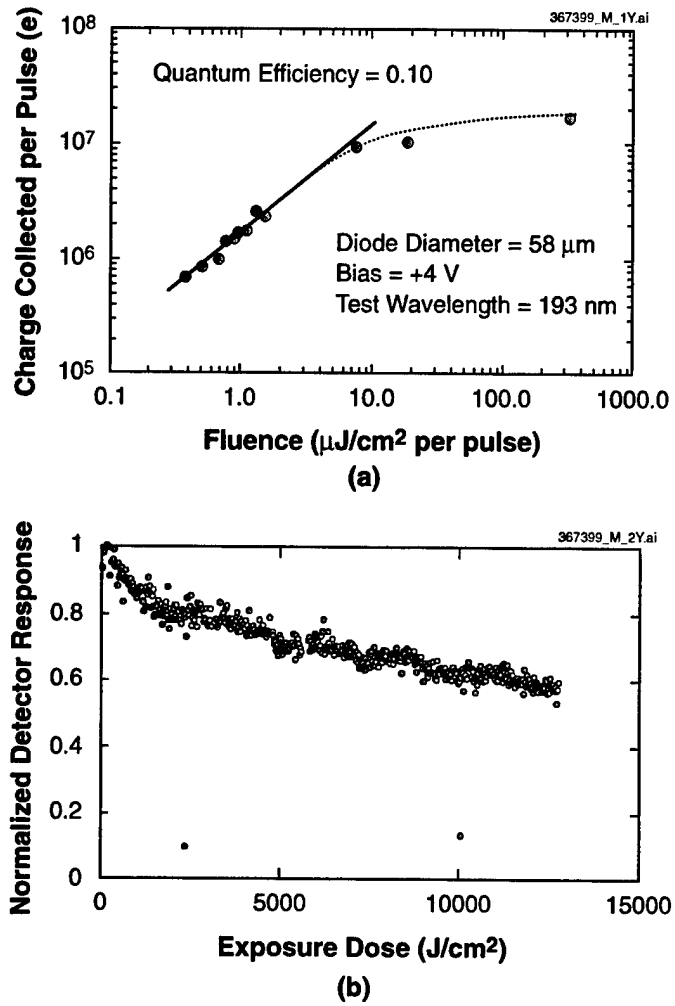

Figure 3-1. (a) Quantum yield and fluence dependence of Lincoln Laboratory buried-channel photodiode measured in photoconductive mode, and (b) normalized quantum yield of diode exposed to increasingly higher exposure doses. Both measurements were made at 193 nm.

ten years of usage at a fluence of 0.1 mJ/cm^2-pulse and with the detector performing several few-thousand-pulse operations each day.

Because of the difficulty associated with direct measurement of aerial images, methods to measure lithographic lens aberrations have been developed that do not require their precise and quantitative measurement. Rather, alternative approaches exist that extract aberration information by measuring focus and/or image placement shifts for a variety of features whose pitches approach λ/2NA and whose

TABLE 3-1

Estimated Signal Levels from an Aperture-Covered Diode Coupled to a CCD*

Fluence (mJ/cm^2-pulse)	Charge Collected (e)	Signal/Noise (Shot Noise Limited)	CCD Well Content
0.5	650,000	810	65% full
0.1	130,000	360	13% full
0.01	13,000	110	1.3% full
0.001	1,300	36	0.13% full

*Wavelength 193 nm, quantum efficiency 0.1, slit width 100 nm, slit length 13 μm, slit transmission 0.5, laser repetition rate 2 KHz, integration time 100 ms (200 pulses), and CCD well capacity 10^7 e.

orientations are varied enough to extract both the even and odd low-order aberrations. These methods preclude the need for apertures smaller than the projected linewidths, such as those that would be necessary to accurately sample the aerial image directly. However, if these image placement measurements are to utilize an *in situ* detector array, the positional accuracy (both in- and out-of-plane) of each sampling aperture would need to be known to within a few nanometers. With this in mind, we elected to target sampling apertures of 100 and 200 nm in width and with in-plane positional tolerances limited by the placement accuracy of the electron beam tool (stitched over several e-beam fields). The residual x, y, and z placement errors would then be accurately mapped once inside the lithographic tool by using the high-precision wafer stage of the tool.

We chose in-situ doped polycrystalline silicon (poly-Si) as our aperture material for several reasons: poly-Si was chosen because a high-resolution poly-Si gate process had already been developed in our facility, and we chose to heavily dope it to prevent charging during electron beam patterning and to reduce grain size and line-edge roughness. Since the area ratios of "open" aperture to poly-Si covered aperture are as high as 1:500 for the smallest apertures, we needed an optical density of at least 5.7 (base 10) in order to limit light leakage through the poly-Si to <0.1% of the total signal. Table 3-2 shows optical density values (base 10) for 120 nm of heavily doped poly-Si at the key lithographic wavelengths, and Figure 3-2 shows the full optical density spectrum for our 120-nm-thick poly-Si material used for the photodiode cover. Note that the dopant-activation anneal significantly impacts the optical characteristics of the material, but that it remains opaque enough at the key wavelengths to provide sufficient light blockage.

TABLE 3-2

Optical Density Values (Base 10) for 120-nm-Thick Layers of Various Forms of Noncrystalline Silicon at the Three Main Excimer Laser Lithography Wavelengths*

Material	157 nm	193 nm	248 nm
MIT-LL in-situ doped poly-Si (as deposited before anneal)	6.6	7.3	7.7
MIT-LL in-situ doped poly-Si (after anneal; used in device)	5.6	6.4	7.0
Amorphous Si [6]	6.7	7.1	7.3
*Our devices used the MIT-LL in-situ doped poly-Si.			

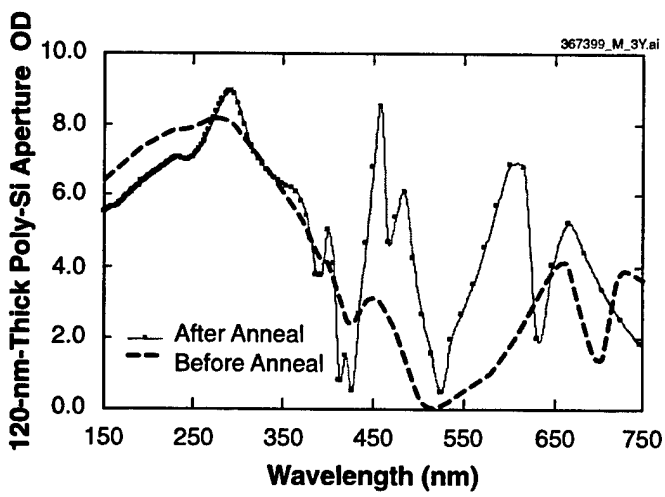

Figure 3-2. Optical density spectrum for polysilicon aperture material used to cover the photodiodes. The polysilicon thickness is 120 nm.

The lithographic process used to fabricate the 100- and 200-nm-wide apertures used a 300-nm-thick layer of Shipley UV-5 resist exposed to 50-keV electrons on a JEOL scanning electron beam lithography system. Figure 3-3 shows a cross section of a test aperture patterned and etched into heavily doped poly-Si.

367399_M_4Y.ai

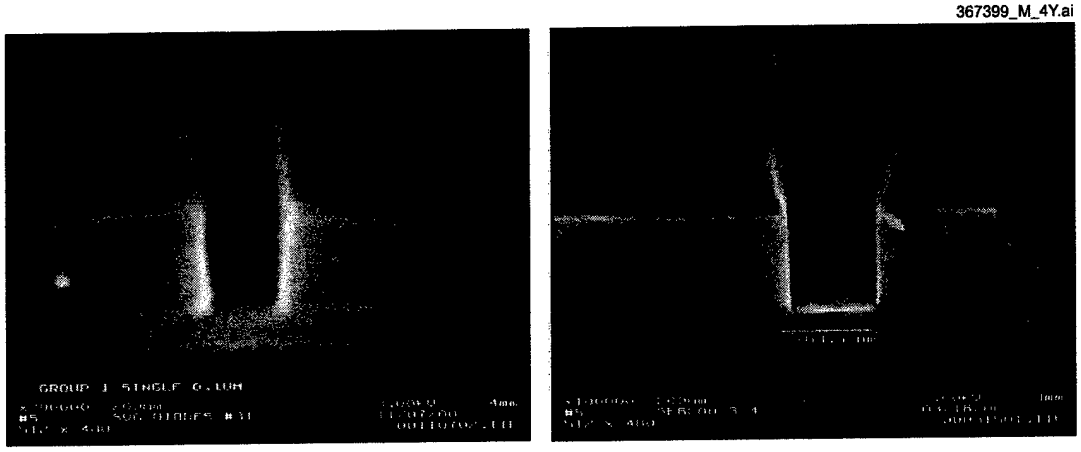

(a) (b)

Figure 3-3. Electron micrographs of sampling aperture fabricated onto the face of the active diodes: (a) 100-nm slit etched into 100 nm of polysilicon (after photoresist stripping), and (b) 200-nm slit etched into 200 nm of polysilicon (before photoresist stripping). In the final devices the polysilicon thickness is 120 nm and the bottom of the slit is comprised of the active photodiode.

The greatest challenge was the monolithic integration of the three primary functions (photodiode, sampling aperture, CCD) into a single device. The approach used had 17 levels of lithography, of which 16 were performed using a 1× optical scanner and one layer using electron beam lithography. Table 3-3 summarizes the process flow, Figure 3-4 shows a close-up schematic of the device, and Figure 3-5 shows a close-up view of a portion of the fabricated device.

Since the use of thin slits or pinholes for aberration extraction and *in situ* lens characterization has already been well established [10][12], we will forgo a discussion of how this device might be applied to this problem, and instead focus on the application of this device as a spatial polarization sensor. Recent trends towards high-NA imaging systems have indicated that there is different contrast for *s*- and *p*-polarization [13]–[15] and that the swing curves may vary as well [15]. In addition, it has been theoretically proposed that polarization masks can be used to enhance imaging performance [16]. For these reasons, control and measurement of spatial variations in polarization may become important as a resolution enhancement tool in the near future. Figure 3-6 shows the measured signal derived from polarized 193-nm illumination for a variety of detector orientations. Since light transmission through the narrow sampling apertures is sensitive to the polarization angle, these devices can be used to quantify and spatially map illumination polarization at the same time that aberrations, image placement, and intensity uniformity are measured.

R. R. Kunz
D. M. Craig
D. J. Landers
M. K. Rose
D. D. Rathman
J. E. Curtin
D. M. Lennon
S. J. Spector
P. J. Daniels
W. H. McGonagle

TABLE 3-3

Process Flow for Monolithic Integration of the CCD, Photodiode, and Sampling Aperture

	Function	Process	Comment*
1	CCD	Implant 1	Channel-stop implant to provide electric-field sink parallel to CCD; local oxidation of silicon for isolation of the active regions
2	Diode	Implant 2	Buried-channel implant (*n*-type) for photodiode charge generation
3	CCD	Implant 3	Scupper implant to shunt photocurrent generated outside active diode or CCD areas
4,5	Diode	Implant 4,5	Diode gradient implants to form an electric-field gradient for electrons to flow from the diode towards the transfer gate
6	CCD	Poly-Si 1	CCD phase 3 and portions of transfer gate and output circuit; oxidize surface of poly-Si 1
7	CCD	Poly-Si 2	CCD phase 2; oxidize surface of poly-Si 2
8	CCD	Poly-Si 3	CCD phase 1 and rest of output circuitry; oxidize surface of poly-Si 3
9	CCD	Contact 1	*N*+ contacts for source and drain of CCD output field-effect transistors
10	CCD	Contact 2	Front-side contact to *p*-type substrate via the channel stop region
11	Diode	Oxide 1	Remove CCD dielectric over diode area and create thin photodiode oxide layer
12	Diode	Nitridation	High-temperature nitridation of active diode area for enhanced UV stability
13	Diode	Poly-Si 4	Pattern 100 nm of doped poly-Si just over active diode area
14	CCD	Contact 3	Make openings in poly-Si 1, 2, and 3 to prepare for metal 1
15	CCD	Metal 1	Contacts and interconnects for CCD
16	CCD	Oxide 2	Cover CCD with low-temperature oxide (LTO) for passivation and protection
17	Diode	Etch	Remove LTO over active diode regions
18	Aperture	Etch	E-beam pattern poly-Si 4 using electron beam lithography
19	Diode	Metal 2	Cover whole device with light-shield metal, except active diode and output contacts
20	CCD	Contact 4	Open contacts for bond pads through the LTO

*Start with unpatterned *p*-type Si(100) wafer coated with CCD dielectric.

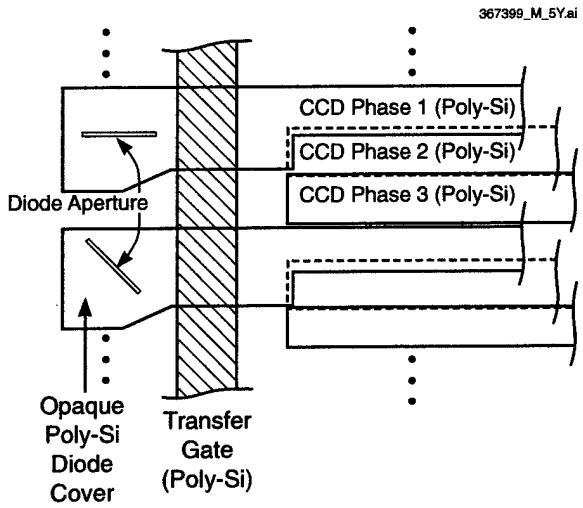

Figure 3-4. Top-down schematic of the photoactive portion of the device.

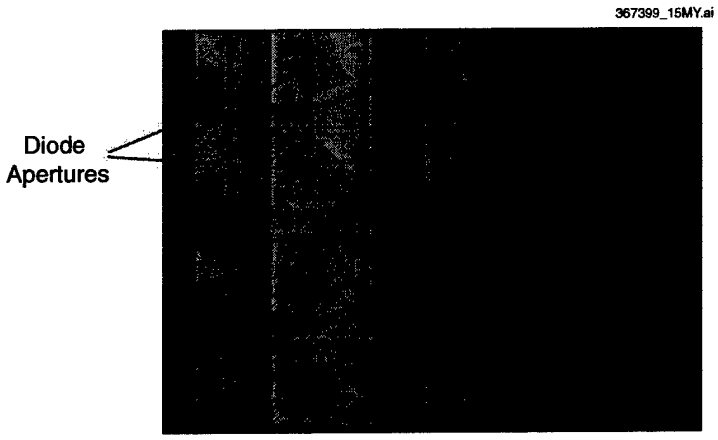

Figure 3-5. Optical micrograph of in-process device corresponding to the schematic shown in Figure 3-4. Only the oxide encapsulation and the aluminum light shield must be added to complete the fabrication.

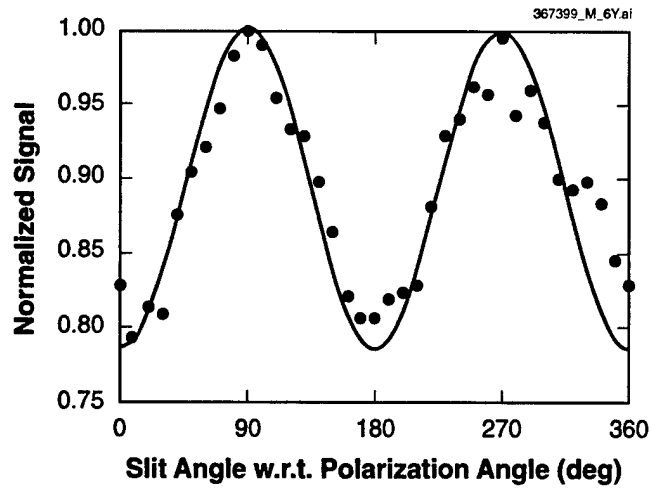

Figure 3-6. Measured (data points) and modeled (smooth curve) detector response to normal incidence polarized 193-nm radiation, as a function of the polarization orientation with respect to the slit. The slit was 200 nm wide and etched into 120-nm-thick poly-Si.

3.2 CHARACTERIZATION OF PAG DECOMPOSITION IN DIFFERENT POLYMER MATRICES AT ADVANCED LITHOGRAPHIC WAVELENGTHS

Lithography at 157 nm represents the next evolutionary step in optical lithography and is recognized as the clear successor to 193- and 248-nm lithography. Resist materials, both polymers and photoacid generators (PAGs), developed for longer wavelengths are highly absorbing with 157-nm radiation and thus prone to increased levels of photochemical reactions [17],[18]. Polymers are known to dissociate into free radical fragments that can then further react to produce chain scission or polymer crosslinking, while the PAG photochemistry is yet unstudied.

One method to probe the PAG photochemistry is through determination of the first-order kinetic rate constant of the radiation sensitive species, the so-called Dill's C parameter [19]. In chemically amplified (CA) resists, this species is the PAG that will generate acid during resist exposure. The exposure kinetics of this transformation are given by Equation (3.1) in which m is the PAG concentration, E is the deposited energy, and C is the exposure rate constant with units of 1/dose.

$$m = e^{-CE} \tag{3.1}$$

Measurement of the Dill C parameter typically involves measurement of some physical quantity directly proportional to *m* as a function of incident dose. Usually these measurements are made at the exposure wavelength under the assumption that the optical properties are directly related to the concentration of PAG compound. However, resist absorbance at the actinic wavelength may not be selective in isolating and measuring only the photoactive species. In CA resists the changes in resist absorbance often do not reflect PAG decomposition, but instead other photochemical transformations such as quinone formation. Fourier transform infrared (FT-IR) spectroscopy, on the other hand, can directly measure changes in the photoactive species by isolating and measuring absorbance peaks unique to it. In addition, antireflective coatings that are transparent to the FT-IR wavelength being monitored can be employed, which mitigates the effect of small changes in resist thickness on the calculated C value during optical exposure.

In this study, the FT-IR measurements were made with a Bruker Equinox 55 FT-IR employing an IRscope II in reflectance mode through a grazing angle objective. Resist thickness was 60–300 nm, spectral resolution was 4 cm^{-1}, and typically 1024 spectra were averaged from each exposure measurement. The Bruker Opus software, which controlled the spectrometer data acquisition and IRscope II, allowed one to measure a predetermined matrix of locations, which in our case corresponded to the location of the UV exposure. The FT-IR reference signal was subtracted from the exposed area signal and integrated from 2080 to 2150 cm^{-1}. The FT-IR absorbance was normalized to the absorbance of the unexposed resist film. The exposure rate constant, the Dill C parameter, was determined with the ProABC lithography simulator by fixing the A value to 0.0 and the B value to the calculated film absorbance. The ProABC software was allowed to determine the best fit of the change in FT-IR absorbance to incident dose.

We employed this method to determine Dill's C parameter for a variety of PAG/polymer films under 157-, 193-, or 248-nm exposure. Four related PAGs were used, di(phenylsulfonyl)diazomethane (DPSD), di(4-methylphenylsulfonyl)diazomethane (DMPSD), di(4-chlorophenylsulfonyl)diazomethane (DCPSD), and di(cyclohexylsulfonyl)diazomethane (DCHSD). The chemical structures are shown in Figure 3-7. All PAGs share a common structure feature, that being the diazomethane moiety, which allows for the ready integration of the diazo absorbance at ~2100 cm^{-1}. The loss of this PAG-specific absorbance can be directly correlated with the photo-induced decomposition of the PAG.

A typical FT-IR spectrum of a PAG/polymer film showing the change in the absorbance at ~2100 cm^{-1} as a function of exposure time is seen in Figure 3-8. Illumination was with a 157-nm wavelength source over a series of exposure doses ranging from 0 to 400 mJ/cm^2. The spectra shown are the difference of the spectra taken at different exposure times subtracted from the fully exposed spectra. The unexposed PAG/polymer film spectra are shown at the back of the graph as spectrum zero. The loss of the diazo peak at ~2100 cm^{-1} is clearly shown with increasing spectra number until complete loss of the diazo peaks occurs at about spectrum 25. The integrated absorbance of the diazo peak was normalized to the initial absorbance and input into ProABC software, specially modified to allow FT-IR absorbance input, along with the incident exposure dose and the appropriate optical parameters.

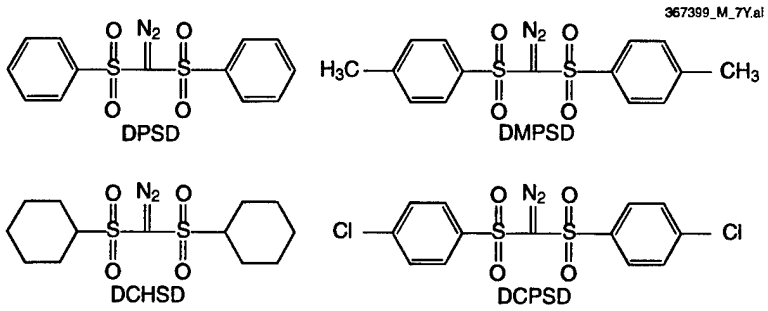

Figure 3-7. Chemical structures of di(phenylsulfonyl)diazomethane (DPSD), di(4-methylphenylsulfonyl)diazomethane (DMPSD), di(4-chlorophenylsulfonyl)diazomethane (DCPSD), and di(cyclohexylsulfonyl)diazomethane (DCHSD).

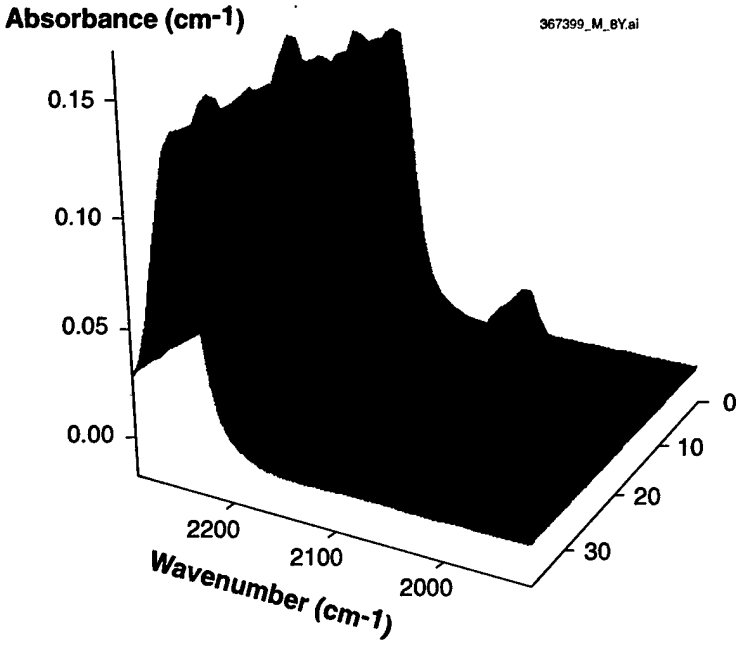

Figure 3-8. Fourier transform infrared spectrum of 10% DPSD in Fox16 (FOX), showing loss of diazo absorbance at 2100 cm^{-1} with increasing exposure dose from back to front.

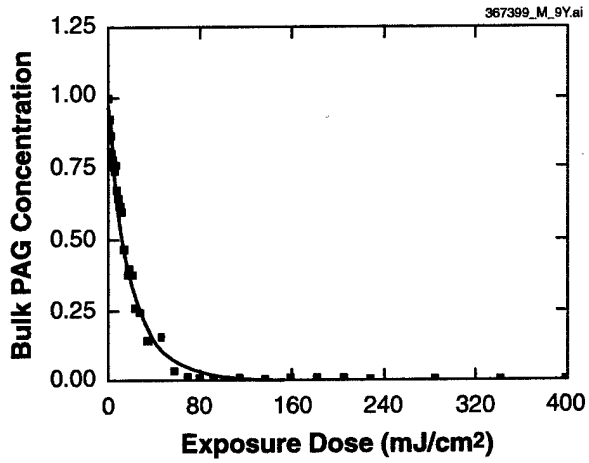

Figure 3-9. ProABC fit for 10% DPSD in FOX with 157-nm exposure.

Four polymers were employed as models for different resists that are commonly used for advanced lithography. Poly(hydroxystyrene) (PHOST) and poly(methyl methacrylate) (PMMA) were selected to represent typical polymer matrices found in 248- and 193-nm resists, respectively. Poly(4-hexafluoroisopropanol styrene) (PHFIPS) was selected to represent the fluoropolymer classes of resists that are being employed in 157-nm resists. Finally, Fox16 (FOX), a hydrogen silsesquioxane, was selected to provide a very low absorbing and assumed inert matrix for PAG decomposition. It is expected that any significant change in the Dill C parameter from that obtained in FOX can be attributed to interactions between the polymer and the PAG.

A typical experiment with 157-nm exposure was to expose a film of 10% PAG in the polymer and measure the change in IR absorbance associated with the diazo moiety. The exposure dose range was from 0 to 400 mJ/cm^2. One additional exposure was made at 5 times the highest dose, 2000 mJ/cm^2, to ensure that full loss of the diazo IR absorbance occurred. The unexposed absorbance was used to set the maximum point for normalized IR absorbance, and the highest exposure dose was employed to fix its zero point. The ProABC fit for 10% DPSD in FOX with 157-nm exposure is shown in Figure 3-9. It can be seen that about 75% PAG decomposition has occurred by 30 mJ/cm^2 and that virtually all PAG has decomposed by 100 mJ/cm^2. The Dill C value determined for this film was 0.057 cm^2/mJ.

The Dill C parameters for 193- and 248-nm exposure were determined in an identical manner, except the dose range was increased to 0–800 mJ/cm^2 and the maximum dose used to set the zero point was scaled accordingly to 4000 mJ/cm^2. The ProABC fit for 10% DPSD in FOX with 193- and 248-nm exposure is seen in Figures 3-10 and 3-11. Figure 3-10 shows that with 193-nm exposure about 75% PAG decomposition has occurred by 30 mJ/cm^2 and that virtually all PAG has decomposed by 150 mJ/cm^2.

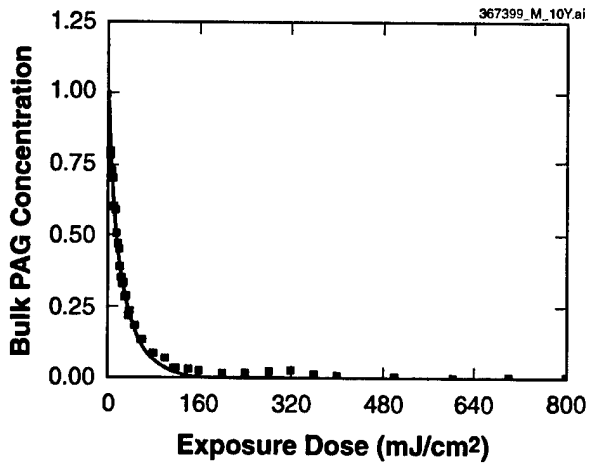

Figure 3-10. ProABC fit for 10% DPSD in FOX with 193-nm exposure.

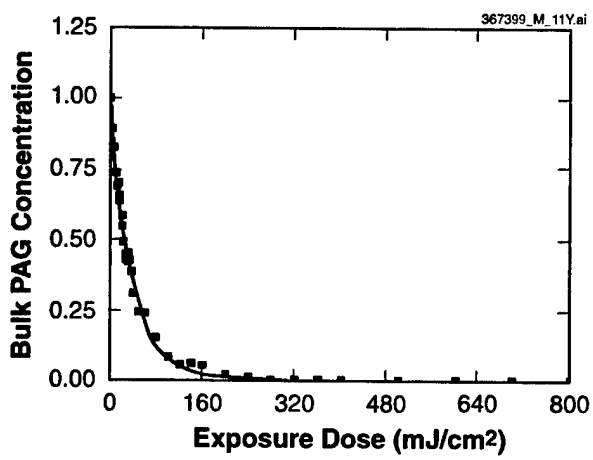

Figure 3-11. ProABC fit for 10% DPSD in FOX with 248-nm exposure.

Figure 3-11 shows that with 248-nm exposure about 75% PAG decomposition has occurred by 60 mJ/cm^2 and that virtually all PAG has decomposed by 200 mJ/cm^2. The Dill C values determined for this film were 0.055 cm^2/mJ for 193-nm exposure and 0.034 cm^2/mJ for 248-nm exposure.

The Dill C values for all PAG and polymer combinations with 157-nm exposure are summarized graphically in Figure 3-12. The FOX inorganic polymer gives the lowest Dill C value with each PAG measured and validates the initial assumption that the low absorbing and assumed inert matrix would give a baseline Dill C value without interaction, whether sensitization or other, from the polymer. The Dill C

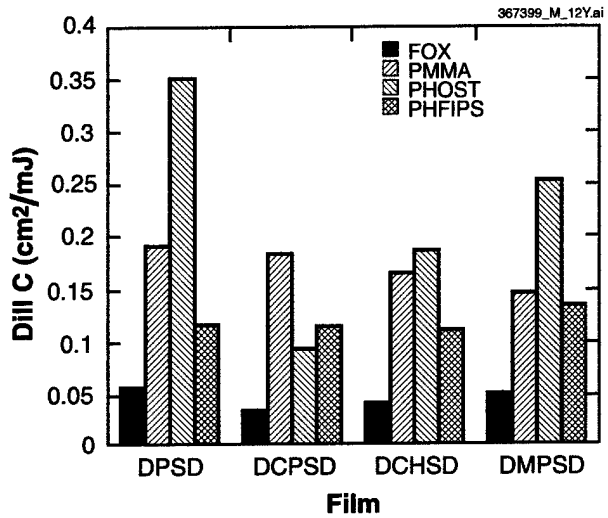

Figure 3-12. Dill C values for all PAG and polymer combinations with 157-nm exposure.

value obtained with FOX is similar for all PAGs and averages to 0.05 cm^2/mJ. This is not surprising in that the 157-nm absorbance for the four PAGs is similar and little difference is expected in the photochemistry of the diazo group. The three organic polymers all give enhanced Dill C values. The Dill C for the PAGs with PHFIPS polymer range from 0.10 to 0.15 cm^2/mJ, a factor of 3 increase relative to the values obtained with FOX. Additional enhancement is seen with PMMA and PHOST polymers where the Dill C value increases to 0.15–0.20 in the PMMA polymer matrix and 0.10–0.35 with a PHOST based film. This is clear evidence that the polymer matrix can lead to increased PAG decomposition by a factor ranging from 2 to 6 times that observed with an inert matrix.

The Dill C values for all PAG and polymer combinations with 193-nm exposure are summarized graphically in Figure 3-13. The FOX inorganic polymer again gives the lowest Dill C values ranging from 0.02 to 0.10 cm^2/mJ. The lowest value is for the nonaromatic DCHSD PAG, and this is consistent with the relatively low absorbance of the PAG at 193 nm. The PMMA polymer gives an enhanced Dill C value ranging from 0.10 to 0.20 cm^2/mJ for all PAGs except the nonaromatic DCHSD PAG, which has a value identical to that of FOX. Both aromatic polymers exhibit a very large enhancement in the Dill C parameter. The enhancement with PHFIPS is from 5 to 10 times with aromatic PAGs and over a factor of 10 for the aliphatic PAG relative to FOX. This enhancement is even more pronounced with PHOST where the increase in the rate of PAG decomposition ranges from a factor of 20 to 40. The enhancement in the PAG decomposition rate that is observed with different organic polymers at 157 nm is magnified many times with 193-nm exposure.

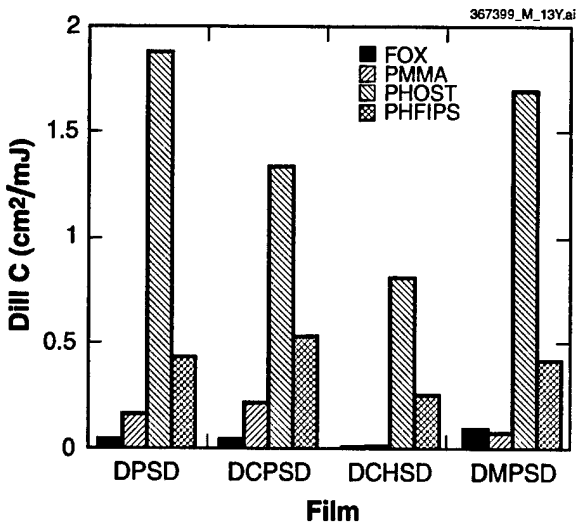

Figure 3-13. Dill C values for all PAG and polymer combinations with 193-nm exposure.

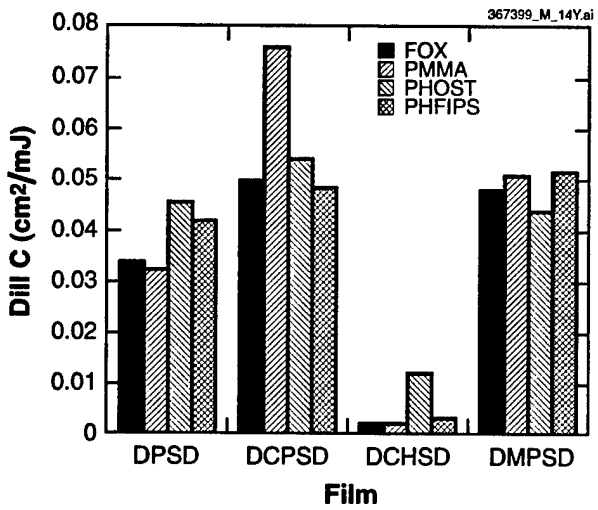

Figure 3-14. Dill C values for all PAG and polymer combinations with 248-nm exposure.

The Dill C values for all PAG and polymer combinations with 248-nm exposure are summarized graphically in Figure 3-14. The nonaromatic PAG again gives the lowest Dill C values typically <0.01 cm^2/mJ, and this is consistent with the relatively low absorbance of the PAG at 248 nm. The three aromatic PAGs give Dill C values ranging from 0.03 to 0.05 cm^2/mJ. Little difference is observed with different polymer matrices, except for DCHSD in PHOST, and it appears that at 248 nm the PAG absorbance alone

determines the PAG decomposition rate. The higher Dill C value for DCHSD in PHOST is consistent with hydroxystyrene based polymers acting to sensitize the PAG.

With both 157- and 193-nm exposure, the FOX inorganic polymer gives the lowest Dill C value with each PAG measured and validates the initial assumption that the low absorbing and assumed inert matrix would give a baseline Dill C value without interaction, whether sensitization or other, from the polymer. The three organic polymers, PMMA, PHOST, and PHFIPS, all give enhanced Dill C values. This is clear evidence that the polymer matrix can lead to increased PAG decomposition by a factor ranging from 2 to 6 times that observed with an inert matrix. Little difference in PAG decomposition is observed with different polymer matrices with 248-nm exposure, and it appears that the PAG absorbance alone determines the PAG decomposition rate.

T. H. Fedynyshyn R. F. Sinta
W. A. Mowers A. Cabral

REFERENCES

1. T. A. Brunner and R. R. Allen, *IEEE Electron Device Lett.* **EDL-6**, 329 (1985).
2. T. A. Brunner, S. Cheng, and A. Norton, *Proc. SPIE* **922**, 366 (1988).
3. J. P. Kirk, G. Kunkel, and A. K. Wong, *Proc. SPIE* **4346**, 8 (2002).
4. H. Nomura, *Proc. SPIE* **4346**, 25 (2002).
5. N. R. Farrar, A. H. Smith, D. R. Busath, and D. Taitano, *Proc. SPIE* **4000**, 18 (2001).
6. R. Korde, *IEEE Trans. Nucl. Sci.* **36**, 2169 (1989).
7. R. Korde, J. Cable, and R. Canfield, *IEEE Trans. Nucl. Sci.* **40**, 1655 (1993).
8. R. Korde and J. Geist, *Appl. Opt.* **26**, 5284 (1987).
9. E. D. Palik, ed., *Handbook of the Optical Constants of Solids* (Academic, New York, 1985).
10. T. Hagiwara, H. Mizutani, N. Kondo, J. Inoue, K. Kaneko, and S. Higashibata, *Proc. SPIE* **4346**, 1635 (2002).
11. W. N. Partlo, C. H. Fields, and W. G. Oldham, *J. Vac. Sci. Technol. B* **11**, 2686 (1993).
12. W. N. Partlo, C. H. Fields, and W. G. Oldham, *Proc. SPIE* **2197**, 585 (1994).
13. D. G. Flagello, A. E. Rosenbluth, C. Progler, and J. Armitage, *Microelectron. Eng.* **17**, 105 (1992).
14. B. W. Smith and J. Cashmore, *Proc. SPIE* **4691**, 11 (2002).

15. T. A. Brunner, N. Seong, W. A. Hinsberg, J. A. Hoffnagle, F. A. Houle, and M. I. Sanchez, *Proc. SPIE* **4691**, 1 (2002).

16. M. Lam and A. Neurether, *Proc. SPIE* **4691**, 437 (2002).

17. T. H. Fedynyshyn, R. R. Kunz, R. F. Sinta, R. B. Goodman, and S. P. Doran, *Proceedings of the 12th International Conference on Photopolymers* (Society of Plastics Engineers, Brookfield, CT, 2000), p. 3.

18. T. H. Fedynyshyn, R. R.Kunz, R. F. Sinta, R. B. Goodman, and S. P. Doran, *J. Vac. Sci. Technol. B* **18**, 3332 (2000).

19. F. H. Dill, W. P. Hornberger, P. S. Hauge, and J. M. Shaw, *IEEE Trans. Electron Devices* **ED-22**, 445 (1975).

4. BIOSENSOR AND MOLECULAR TECHNOLOGIES

4.1 EEL HIGH-ENERGY-DENSITY BIOFUEL CELL

Biologically based fuel cells with very high energy densities are being developed using an approach termed EEL (Engineered Electrocyte Layers). The resulting biofuel cells have approximately 60× greater energy density than conventional batteries and should be inexpensive to produce and to refuel. Potential applications for these refuelable, high-energy-density power sources include mobile electronic devices, long-lived deployable sensors, soldiers' field gear, and electric vehicles. In a previous report, we demonstrated the critical steps in engineering *Caulobacter* bacteria for biofuel cells and showed that the bacteria can be maintained under typical biofuel cell conditions for over two months [1]. Here, we describe further proof-of-concept experiments.

Important steps in the genetic engineering of *Caulobacter* are illustrated in Figures 4-1 and 4-2. Following our initial demonstratons [1], we used genomic PCR to clone the DivJ, HfaC, and HfaD stalk-tip targeting signals. Then we fused each of the signals in frame with either end of GFP using splicing by overlap extension. Some of the resulting genes are shown in Figure 4-1. Next, we inserted these spliced

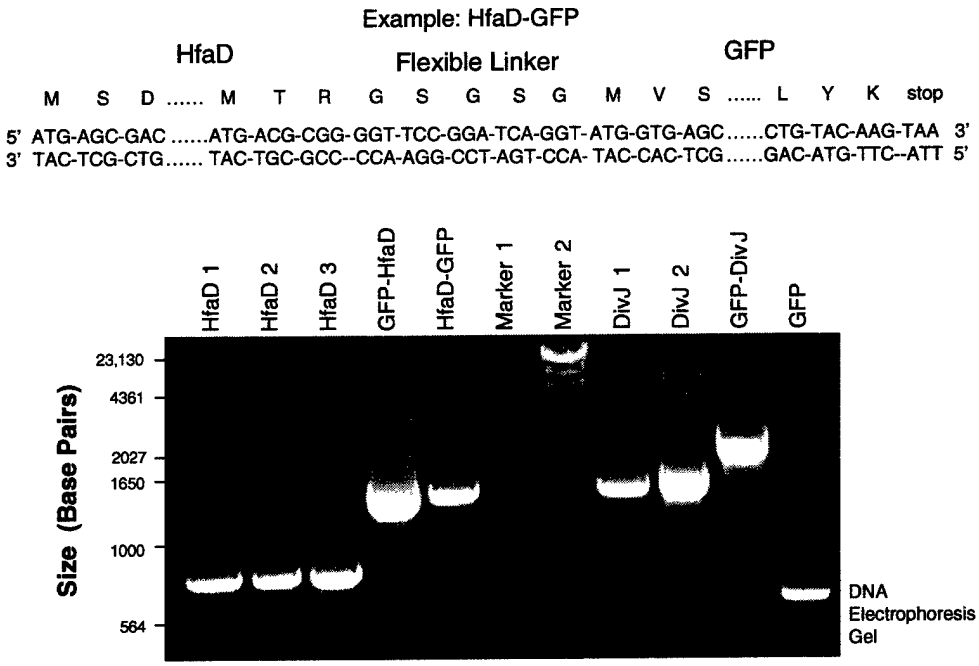

Figure 4-1. HfaD targeting signals spliced to GFP gene.

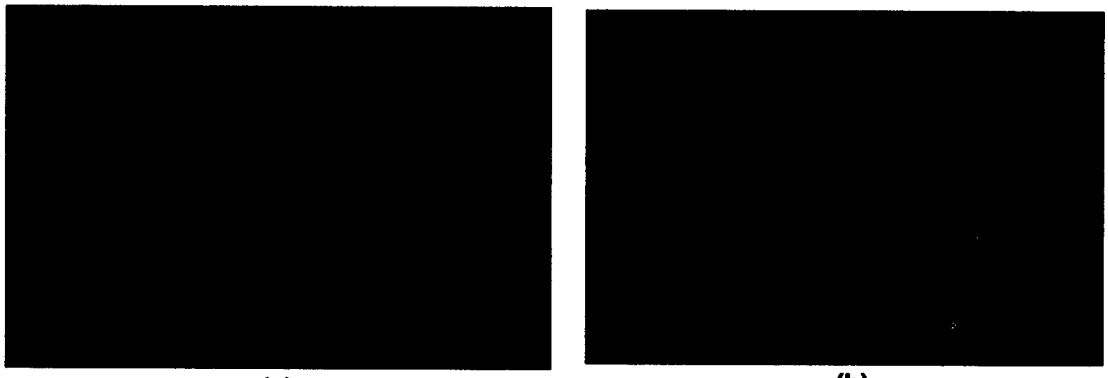

(a) (b)

Figure 4-2. Photographs of genetically engineered Caulobacter with targeted GFP, showing (a) DivJ signal localized to the stalk tip and (b) HfaD signal not localized to the stalk tip. Images were obtained with a 1000× fluorescent microscope.

genes into the Invitrogen pCX-TOPO DNA delivery vector. Finally, we transformed the completed DNA vectors into *Caulobacter*. Figure 4-2 presents photographs of some of the genetically engineered bacteria as viewed with a fluorescent microscope. The DivJ signal targeted GFP to the stalk as intended, leading to bacteria that appear dark except for a glowing point at the tip. In contrast, HfaD was less reliable as a targeting signal and frequently failed entirely, as shown in the photograph in which the entire bacterial body appears to glow brightly. HfaC proved to be even less suitable as a targeting signal. Thus, our experiments have identified DivJ as the best stalk targeting signal and demonstrated that it can be spliced onto a gene of our choice.

Once the genetic engineering of *Caulobacter* is completed, it can be tested as shown in Figure 4-3. Using a pH-sensitive fluorescent dye such as SNARF-1 [2] and a fluorescent microscope, it should be possible to observe the pH gradient caused by proton pumping in the engineered bacteria. Amantadine [3] can be used to selectively inhibit the stalk-tip pores, or cyanide [4] can be employed to selectively inhibit the proton pumps in the bacterial body, and the results can be visualized with the fluorescent dye. We should also be able to make direct electrical measurements of the proton pumping by attaching a large number of bacteria to a surface and measuring the proton current with a Cytosensor probe [5] or microelectrode detector [6],[7]. This work is under way.

To further demonstrate the feasibility of the EEL concept, we have modeled the performance of the bacteria. One example of these modeling studies is Figure 4-4(a), which demonstrates that the desired proton gradients can be maintained in *Caulobacter* bacteria with stalks of the appropriate length. Figure 4-4(a) plots the proton current density that can be pumped by bacteria [8],[9] and compares it with the proton current density predicted to flow by diffusion [10] down bacterial stalks of a given length. Good gradients can be maintained for stalks that are ~10 μm long, such as have been easily produced in

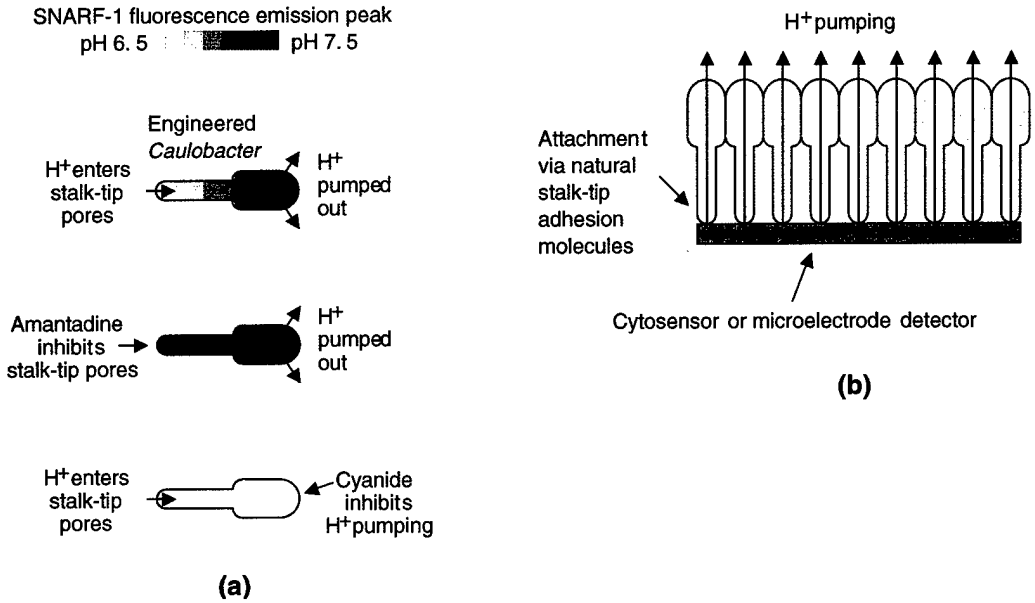

Figure 4-3. Test of engineered bacteria with (a) fluorescence microscopy with SNARF-1 or other pH-sensitive dyes and (b) direct measurement of proton pumping.

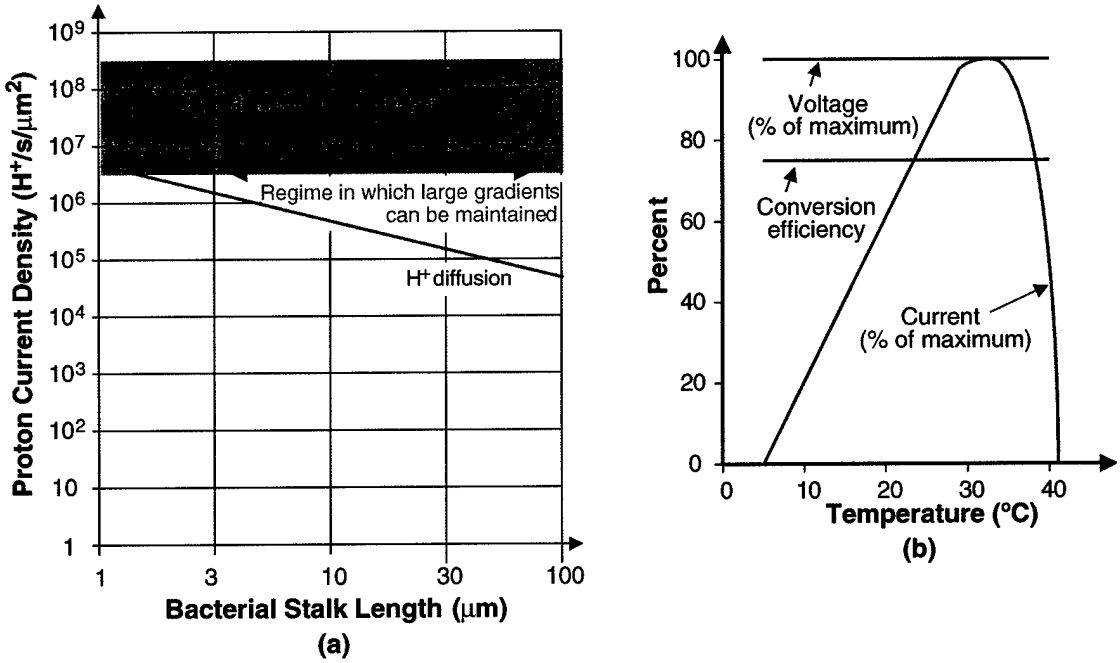

Figure 4-4. Modeled performance of bacteria: (a) proton current density in relation to stalk length, and (b) temperature dependence.

our experiments. Figure 4-4(b) shows another example of the modeling studies, namely, a graph of the temperature dependence of EEL performance. The biofuel cell output voltage depends on the membrane potential of individual bacteria and should remain approximately constant despite temperature changes. Likewise, the chemical-to-electrical energy conversion efficiency is a fundamental property of the biochemical pathway for breaking down fats and sugars, so it should also remain essentially constant over a wide temperature range. In contrast, the electric current output depends on the rate of bacterial metabolism and hence should have approximately the temperature dependence shown in Figure 4-4(b). Since the temperature dependence has a broad peak and is centered at approximately room temperature, the bacterial biofuel cell should be fine for a number of applications. If operation outside that temperature range is required, one could employ insulation, heat fins (for cooling), the natural heat production of the bacteria (for warmth), or active temperature control. Alternatively, one could use another bacteria species, since different species of bacteria can thrive at temperatures ranging from –5°C to 110°C [11].

Attachment and maintenance of *Caulobacter* on surfaces is a critical requirement for using the bacteria in a biofuel cell. Bacteria were deposited onto glass and plastic surfaces and kept in Petri dishes of culture medium. The bacteria were maintained at room temperature in a desk drawer in the biology laboratory; the fact that the bacteria require virtually no maintenance is a great advantage for their use in biofuel cells. Four different strains of *Caulobacter* were tested (CB2A, CB15, CB15N, and YB767), and the results for the best strain (CB2A) are shown in Figure 4-5. These photographs reveal that the bacteria formed self-organized, tightly packed monolayers on both glass and plastic surfaces. The bacterial monolayer was somewhat more organized on the glass than on the plastic, perhaps because the glass had a smoother surface than the plastic. The bacteria remained very firmly attached to the surfaces even after vigorous shaking. After about two weeks, division of the *Caulobacter* had created a cloud of new bacteria that could not find room to attach on the surface. This cloud of bacteria above the surface began to obscure the view of the bacteria on the surface.

Thus, several key principles for the EEL biofuel cell have been demonstrated. Because such cells should have up to 60× higher energy densities than batteries and could be easily refueled with any organic matter, they have the potential to revolutionize energy storage for a wide variety of military and commercial applications.

T. H. Rider
T. L. Schmidt

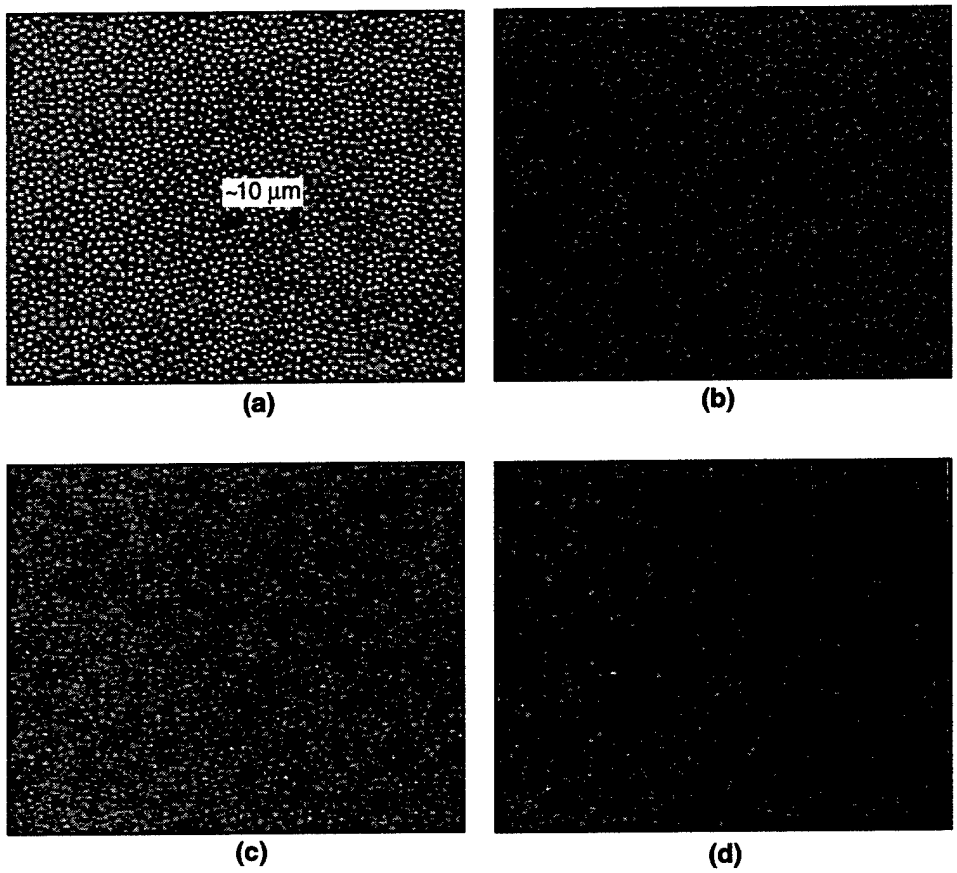

Figure 4-5. Photographs showing attachment and maintenance of Caulobacter (a) on glass after 1 day, (b) on glass after 12 days, (c) on plastic after 1 day, and (d) on plastic after 12 days. Images were obtained with a 400× phase-contrast microscope with a charge-coupled device camera.

REFERENCES

1. Solid State Research Report, Lincoln Laboratory, MIT, 2002:3, p. 19.
2. R. P. Haugland, ed., *Handbook of Fluorescent Probes and Research Chemicals,* 7th ed. (Molecular Probes, Eugene, OR, 1999).
3. K. C. Duff and R. H. Ashley, *Virology* **190**, 485 (1992).
4. L. Stryer, *Biochemistry*, 4th ed. (W. H. Freeman, New York, 1995).

5. H. M. McConnell, J. C. Owicki, J. W. Parce, D. L. Miller, and G. T. Baxter, *Science* **257**, 1906 (1992).

6. L. J. Breckenridge, R. J. A. Wilson, P. Connolly, A. S. G. Curtis, J. A. T. Dow, S. E. Blackshaw, and C. D. W. Wilkinson, *J. Neurosci. Res.* **42**, 266 (1995).

7. I. D. Hentall, *J. Neurosci. Methods* **40**, 181 (1991).

8. T. Kuroda, N. Okuda, N. Saitoh, T. Hiyama, Y. Terasaki, H. Anazawa, A. Hirata, T. Mogi, I. Kusaka, T. Tsuchiya, and I. Yabe, *J. Biol. Chem.* **273**, 16897 (1998).

9. K. B. Anderson and K. von Meyenburg, *J. Bacteriol.* **144**, 114 (1980).

10. G. W. Castellan, *Physical Chemistry*, 3rd ed. (Addison-Wesley, Reading, MA, 1983), p. 791.

11. M. T. Madigan, J. M. Martinko, and J. Parker, *Brock Biology of Microorganisms,* 8th ed. (Prentice Hall, Upper Saddle River, NJ, 1997).

5. ADVANCED IMAGING TECHNOLOGY

5.1 CLOCK TREE TECHNIQUE FOR ELECTRICAL DISTRIBUTION OF SIGNAL EXPOSURE CONTROL FOR FOCAL PLANE ARRAYS

Large-format solid state imagers with exposure times below a nanosecond do not exist. High-speed imaging is done either with film or specially adapted tube-based technology. These approaches suffer from low dynamic range, low contrast, high noise, and inflexible operation.

For high-speed, large-format detectors with millions of pixels, the trigger clock must be distributed to all pixels such that the sampling occurs effectively simultaneously. For detectors with dimensions of multiple centimeters, the time to propagate across a chip is hundreds of picoseconds. Parallel clock distribution either electrically and/or optically is needed to reduce the skew. Possible approaches for distributing the clock electrically are the H-tree or row-column-tree type structures. This work describes an approach and implementation using an H-tree clock distribution network designed specifically for high-speed imaging in relatively large area arrays.

Figure 5-1 illustrates the electrical clock H-tree architecture. In this technique, a trigger clock driver sends the signal down lines that continue to branch until the signal reaches all pixels (or an array of pixels that can be easily driven) almost simultaneously since the electrical path lengths are identical. A branch point along the signal chain may contain a repeater buffer that sharpens the pulse edge. Also, by locating the repeaters every few tenths of a millimeter, the short signal line length in between branches can be treated as lumped-circuit elements.

As shown in Figure 5-2 for passive clock trees, the signal is attenuated after several millimeters for typical 0.18-μm bulk CMOS processes. To overcome the attenuation, an active buffer (repeater) is placed every few millimeters, depending on the fanout, to sharpen the pulse edge. The active repeater adds both a

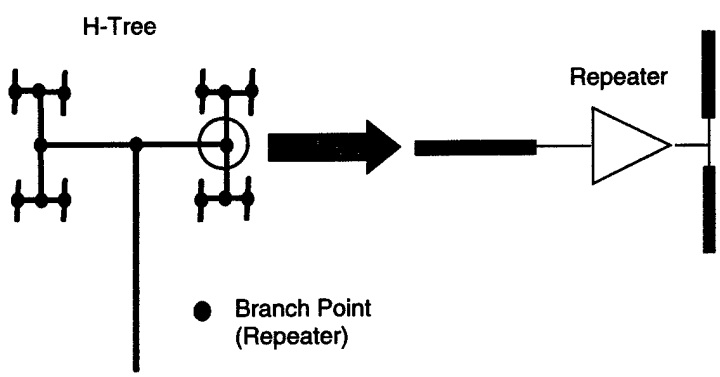

Figure 5-1. Example of H-tree clock distribution.

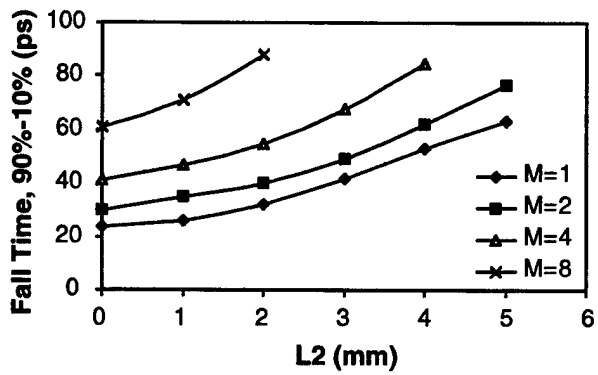

Figure 5-2. Signal fall time vs interconnect length L2 between repeaters for various fanouts M. Simulation done using a 0.18-μm bulk CMOS technology.

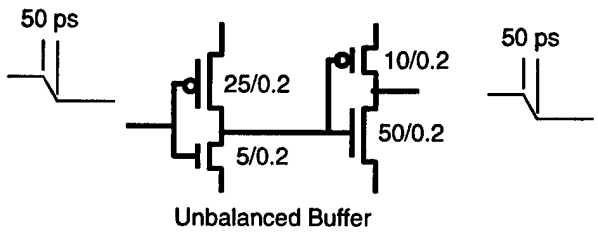

Figure 5-3. Unbalanced buffer/repeater; circuit numbers to the right signify width/length for the transistors.

fixed and random time delay (jitter). Calibration techniques can be used to remove the fixed delay. The tree structure should be optimized to limit the random jitter. Even so, for relatively large chips of a few centimeters, the number of repeaters needed to distribute the clock to the final array of pixels will be of the order of 20.

The standard deviation for the total jitter should be <100 ps to be useful for applications with integration times of this order. For example, a 0.18-μm bulk CMOS process will have gate delays of ~28 ps. Assuming the jitter of one repeater is 10% of this, and that the jitter is independent for each repeater, the standard deviation for the path is ~12 ps, or for the worst case, three standard deviations at 36 ps.

Distributing just the falling (rising) edge allows the use of an unbalanced inverter-repeater that is optimized for generating a fast falling (rising) edge as opposed to a symmetric inverter that generates both rising and falling edges. Transferring both edges can compromise both speed and device area as well as increase jitter. Figure 5-3 shows the unbalanced inverter with asymmetric *n*- and *p*-channel transistors.

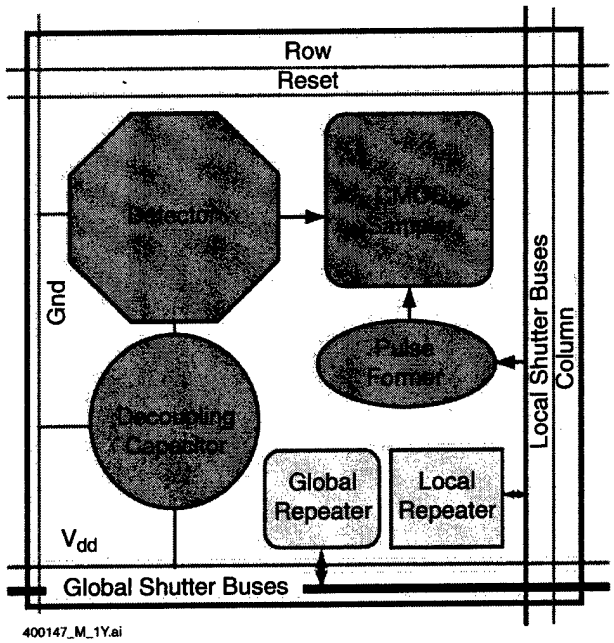

Figure 5-4. Pixel architecture showing support circuitry for distribution of the local and global clock.

The H-tree global distribution network with the periodic inverter-repeater buffers delivers the fast edge signal to a local neighborhood array of pixels, e.g., 8×8 array. Within the local neighborhood, similar circuits can be used to deliver this same edge to all 64 pixels in a fan-out pattern without the need for the H-tree. Both the global repeaters and local drivers must be constructed within the pixel array architecture with some portion of each pixel designated for either global or local distribution functions.

Besides the active repeater for local and global clock distribution, other circuit functions can be generated using the pixel circuitry, as illustrated in Figure 5-4. These include pulse forming for integration control. The exposure is set by the time between the rising and falling edge of the clock. In one particular clock implementation, only the falling (rising) edge of the clock is transferred through the tree with the rising (falling) edge being generated locally to give the complete pulse that determines the integration time for the array of pixels at the end point of the clock tree. Thus, the H-tree distribution network delivers a falling edge to a local group of pixels, where the pixel circuitry at that location is used to create both the rising edge and the pulse width to set the integration time.

A prototype 64×64 (30-μm pixel) high-speed CMOS imager is currently being designed for fabrication using the 0.18-μm bulk CMOS mixed-mode process from a silicon foundry. This imager incorporates the H-tree clock distribution architecture detailed above. In addition to the H-tree repeater elements, the pixel architecture includes both a high-speed photodetector and sampling circuit capable of 100-ps integration times. The design of these elements, alluded to in Figure 5-4, will be detailed in future

reports. Using a fast-pulse laser or diode light source one should be able to determine both global and local skew across the imager due to transistor variations throughout the pixel array. In addition, this prototype imager has a number of break-out test circuits that will be able to measure skew directly between neighboring pixels with different electrical paths of identical length.

R. Berger
D. D. Rathman
R. K. Reich

6. ANALOG DEVICE TECHNOLOGY

6.1 ARCHITECTURE FOR A TYPE-II QUANTUM COMPUTER COPROCESSOR

An architecture that we have adopted for the development of a Type-II quantum computer (T2QC) [1] is reported here. Following a very brief description of the T2QC, we describe what a direct implementation of the standard architecture would look like and why it is a poor match to the requirements and characteristics of quantum computational hardware. We then describe our architecture for a quantum coprocessor for a T2QC and enumerate its advantages.

In what we will call a "conventional" quantum computer, computations are performed as a sequence of coherent quantum transformations applied to a set of entangled quantum bits (qubits) [2]. Those qubits are set into a specific initial quantum configuration, typically a uniform superposition of all possible states, and at the end of the complete sequence of quantum operations, the states of the qubits are measured to determine the answer to the problem. Only specific algorithms can be implemented, because the final quantum state must be an eigenstate representing the answer or a superposition of a small number of eigenstates representing possible solutions. An example is Shor's algorithm [3] for factoring numbers, such as those used as public keys in RSA encryption.

The key observation for our present purposes is that such a quantum computer will provide performance that is superior to that of a classical computer only for relatively large problems, for example, numbers with more than 600 bits in the case of Shor's algorithm (we chose 600 bits because it lies just ouside the range of numbers that have been factored by classical computers). Such problems require large numbers of qubits, e.g., $\sim 10^6$ for Shor's algorithm applied to 600-bit numbers, whose quantum states are entangled—and remain coherently entangled—over long sequences of quantum logic operations. Thus, conventional quantum computers make severe demands on quantum coherence, both spatially and temporally. These demands are vastly beyond the current state of the art for any quantum computer implementation.

An alternative approach to quantum computation is the T2QC. Its application space is quite different from that of the conventional quantum computer; it can solve certain nonlinear partial differential equations that describe flows and interactions of particles in fluids. A T2QC on the scale of only tens or hundreds of qubits may be able to achieve a practical advantage over conventional computers. Moreover, the sequences of coherent quantum operations in a T2QC are quite short. Thus, the demands on spatial and temporal coherence are far less than with a conventional quantum computer.

The T2QC is the quantum extension of the lattice Boltzmann model (LBM) version of a lattice-gas cellular automaton (LGCA) [4]. The LGCA, whose architecture is illustrated in Figure 6-1, comprises a lattice of "nodes," each of which represents information about the particles at an idealized point in space. Specifically, the absence or presence of a particle that is moving with a velocity proportional to the distance to another node is stored in a binary "cell" within the node. The computation proceeds in

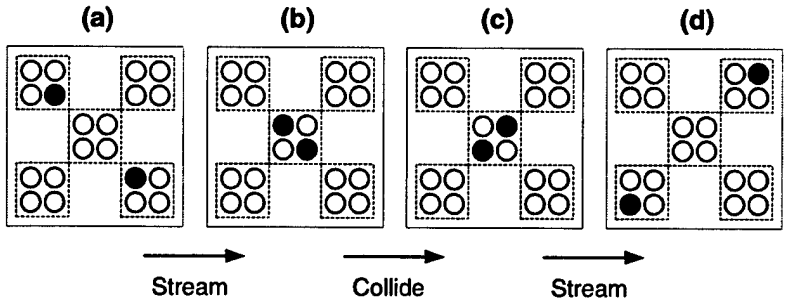

Figure 6-1. Illustration of lattice-gas cellular automaton for the case of a square lattice with particle motion to nearest neighbors only. (a) Five nodes, including a central node and its four nearest neighbors. Each node comprises four cells, shown as circles, corresponding to particle velocities toward the upper right, lower right, lower left, and upper left. The cells are drawn within the node to indicate the corresponding particle velocity and darkened to indicate the presence of a particle This example starts with one particle in the upper-left node that is moving downward to the right and one particle in the lower-right node that is moving upward to the left. (b) Result of the first streaming operation: the two particles have moved to the central node and occupy cells with the same orientation since the particles still have the same velocity. In this example no particles have moved into any of the corner nodes from nodes beyond those shown here. (c) State after a collision computation. In this example, the two particles have changed direction, with one now moving upward to the right and the other downward to the left. (d) State after the next streaming operation, again assuming that no particles enter from nodes beyond those shown. This alternating sequence of steps is repeated many times for the entire lattice of nodes.

alternating steps called "streaming" and "collision," as described in the caption to Figure 6-1. Streaming accounts for the transport of particles from one location (node) to another, while collision represents the interaction (scattering) of particles within a spatial region. Despite what would appear to be the extreme oversimplification of this model of a fluid, LGCAs have successfully solved complex problems in fluid dynamics.

The LGCA represents particle density in a very coarse grained way, namely, present or absent (binary). The LBM uses a finer-grained representation with each cell storing the density of particles with a specific velocity. In the case of a T2QC that implements a quantum LBM, the density is represented by the expectation value of a qubit, that is, the probability of finding it in the '1' state.

In the T2QC, streaming operations are carried out by classical transport of probability values between nodes, while collision operations are carried out by quantum-coherent operations on the quantum states of the nodes. The implementation architecture usually proposed calls for a large number of small quantum computers, each just large enough to store the state of one node, arrayed out with classical interconnects to implement the streaming operations. Figure 6-2 shows such an architecture for a direct electronic circuit implementation of a T2QC corresponding to the lattice shown in Figure 6-1. As indicated in the right-hand portion of Figure 6-2, each node requires the following functional blocks:

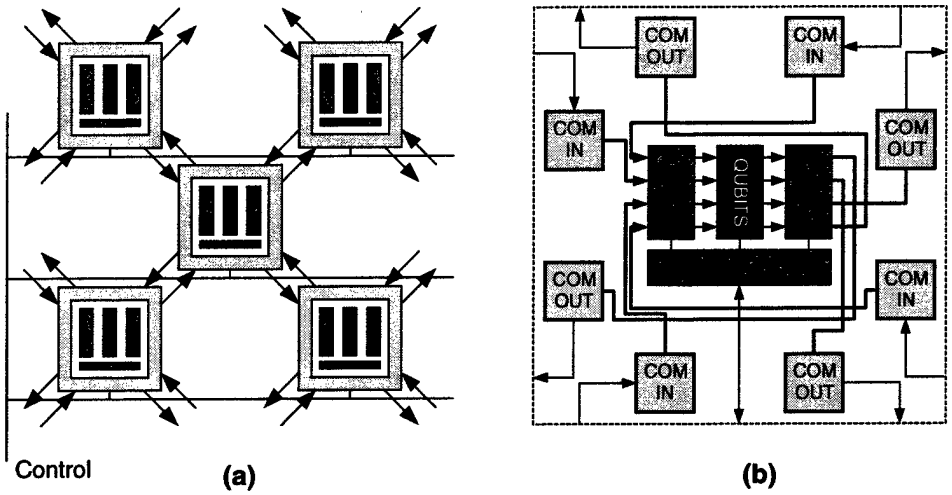

Figure 6-2. Illustration of architecture of a direct implementation of a Type-II quantum computer (T2QC). (a) Lattice of quantum nodes and the communication paths among them. Except for global control signals, each node communicates only with its neighbors (nearest neighbors only in this example). (b) Functional blocks needed in each node.

Control. The control block regulates the functions of all the other blocks.

Communication-in. This block performs its part of the streaming operation by receiving probability values from neighboring nodes of the lattice.

Input Setup. This block sets each qubit in the node to the superposition state representing the precollision occupation probability.

Qubits. The qubits carry out a quantum computation of the collision operation using an interaction Hamiltonian provided by the control block.

Output Sensing. After the quantum operations have been completed, the output sensing block performs a measurement on the qubits. In order to obtain output probability values, the process of initializing the qubits, applying the collision Hamiltonian, and measuring the final qubit states has to be repeated many times, with the statistics being accumulated in the output sensing block.

Communication-out. After a complete set of collision computations has been performed, this block performs its part of the streaming operation by transmitting the output probability values for each cell of the node to the corresponding neighboring node.

This direct implementation architecture is very poorly matched to the characteristics of quantum computational blocks. The problem stems from the huge amount of nonquantum support circuitry required for communication, control, and conventional computation. Some of the problems are as follows: (1) There are eight channels carrying either analog or multi-bit digital data between one node and its neighbors. If

digital communication is used, then many wires are needed, e.g., 64 for 8-bit resolution in the probability values. (2) The input-setup block must generate the required control signals to initialize the qubits. If analog communication is used, then it will have to perform analog computations, which are hard to define and control. If digital communication and computation are used, then a digital-to-analog converter (DAC) will be needed to generate the actual qubit control signals. (3) The output-sensing block has to accumulate statistics, which requires a multi-bit counter for each qubit. If analog communication is used, then the communication-out block needs a DAC. (4) The area consumed by this nonquantum circuitry would dwarf that used for the qubits. Even worse than the waste of area would be the excess power dissipation on a chip whose quantum devices require milli-kelvin temperatures, and the huge amount of coherence-destroying electrical noise generated by the nonquantum circuitry.

Therefore, we have conceived an alternative architecture for a T2QC that overcomes the deficiencies of the direct implementation architecture. The new architecture arises from the following observations: the exponentially hard part of the computation, the part that can take advantage of quantum computation, is the collision calculation; and a classical computer can store the nodal probabilities, perform the streaming operation, and even compute the biases required to initialize the qubits.

From these observations, we were led to design a quantum coprocessor, as illustrated in Figure 6-3. This chip comprises an array of individual quantum nodes, each corresponding to the qubits block in Figure 6-2 and containing a set of entangled qubits. These quantum nodes are initialized to the same starting states, subjected to the same interaction Hamiltonian, and measured in parallel. The qubits in each node, of course, have independent probabilities of being found in the '0' or '1' state. The output sense circuit simply has to compile the statistics to determine the output probability values from the collision operation.

The architecture of the quantum coprocessor is much simpler and more efficient than that of the direct implementation. No internodal communication is required; it is handled off-chip by a classical computer. The setup and control signals are uniform across the chip, and the signals can be computed and generated off-chip. The chip contains primarily quantum circuitry; all nonessential power dissipation has been moved off the chip. Similarly, except for circuitry needed to compile the output probabilities, all digital circuitry—and its associated noise—has been moved off chip. The circuitry that does remain is shut off during the quantum operations.

The coprocessor also provides the flexibility of trading off spatial and temporal parallelism. For example, if the desired accuracy in the output probability values requires 40,000 measurements, but the coprocessor has only 1000 quantum nodes, then the coprocessor operation can be repeated 40 times, with the external classical computer combining the results. This flexibility also allows for the staged development of the coprocessor. A prototype coprocessor can demonstrate the full T2QC computation with as few as *one* quantum node with as few as two coherent qubits, with all of the statistics being compiled externally.

The technology—quantum or classical—that is chosen in building a computer for modeling fluid flow will be guided by the key trade-off between cost and performance. For example, if the algorithm

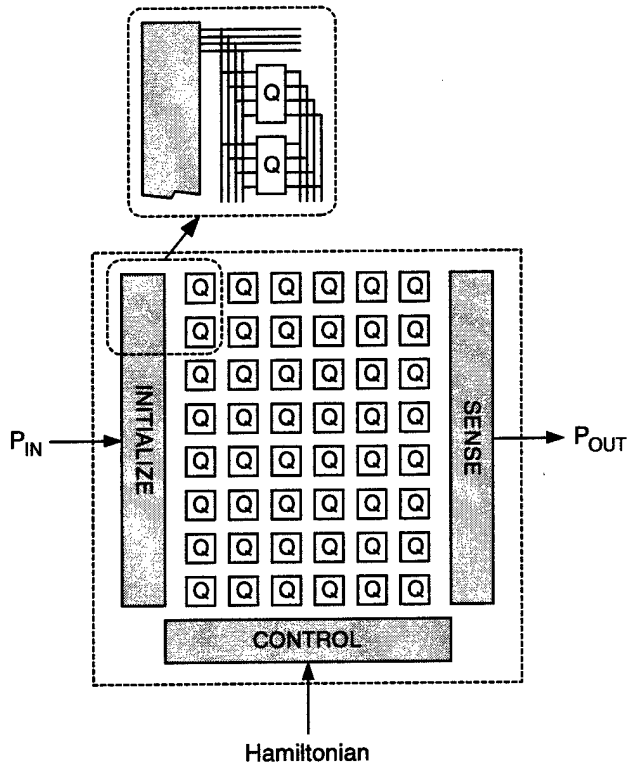

Figure 6-3. Architecture of quantum coprocessor for a T2QC. Each box labeled Q represents a complete quantum node containing a number of coherently coupled qubits (four for the example shown in the inset). The nodes are identical, and they are operated in parallel.

requires relatively few cells per node, then classical implementations of the collision operation could be less costly to implement than quantum implementations. However, the size of the classical look-up table for collisions in larger nodes grows exponentially with the number of cells in the node, rapidly outpacing the capacity of classical storage. It is in this regime that a quantum implementation of an LBM would be most likely to outperform an implementation based solely on classical digital logic.

An important caveat to mention, however, is that no T2QC algorithms are currently known that work with large numbers of cells per node (>10). If the quantum coprocessor architecture we propose encourages development of such algorithms, the result could be a small-scale quantum computer that vastly outperforms classical computers to solve important problems in fluid dynamics.

J. P. Sage
K. K. Berggren

REFERENCES

1. J. Yepez, *Int. J. Mod. Phys. C* **12**, 1273 (2001).

2. M. A. Nielson and I. L. Chuang, *Quantum Computation and Quantum Information* (Cambridge University Press, New York, 2000).

3. P. Shor, *Proceedings of the 35th Annual Symposium on Foundations of Computer Science* (IEEE Computer Society, Los Alamitos, CA, 1994), p. 124.

4. D. A. Wolf-Gladrow, *Lattice-Gas Cellular Automata and Lattice Boltzmann Models: An Introduction* (Springer, New York, 2000).

7. ADVANCED SILICON TECHNOLOGY

7.1 INHERENTLY PLANAR FULLY DEPLETED SILICON-ON-INSULATOR ISOLATION

Any technique used to isolate fully depleted silicon-on-insulator (FDSOI) transistors must satisfy electrical and packing density requirements in order to fabricate dense integrated circuits with low off-state leakage. Three isolation techniques have been applied to FDSOI: local oxidation of silicon (LOCOS), mesa island definition, and shallow trench isolation (STI). Mesa isolation is the most frequently used technique, since island-island spacing can be reduced to 0.5 μm and plasma etches provide a uniform process. However, sidewall implantation of mesa-isolated islands or sidewall rounding techniques are required to suppress sidewall leakage caused by wraparound of the polysilicon gate that causes a reduction in the threshold at the island edge [1]. Care is required to avoid excessive etching of the buried oxide during processing; an extreme example of this effect is shown in Figure 7-1. The premature turn-on of the parasitic edge transistor of a mesa-isolated *n*-FET is shown in Figure 7-2. STI is a very promising technique but one that requires careful control of chemical-mechanical planarization (CMP) when applied to FDSOI processes with SOI thicknesses as small as 40 nm. The recent development of a low-temperature oxide-oxide bond process [2] permits an alternate approach to FDSOI isolation by defining the SOI into islands after completion of conventional circuit fabrication.

FDSOI transistors were fabricated on 150-mm-diam SOI wafers with 200-nm buried oxides. The initial 200-nm-thick SOI layers were thinned to 45 nm by oxidation. After a 4-nm gate oxidation each wafer was implanted with BF_2 or phosphorus to dope the SOI and form either *n*- or *p*-FET transistors. After deposition of 200-nm polysilicon and gate definition, the source-drain extensions were implanted,

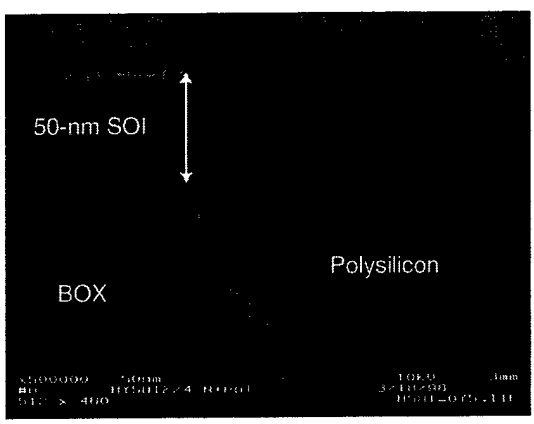

Figure 7-1. Scanning electron micrograph showing penetration of polysilicon gate into buried oxide (BOX) due to erosion of the BOX during processing. The wraparound of the silicon-on-insulator (SOI) reduces the edge threshold.

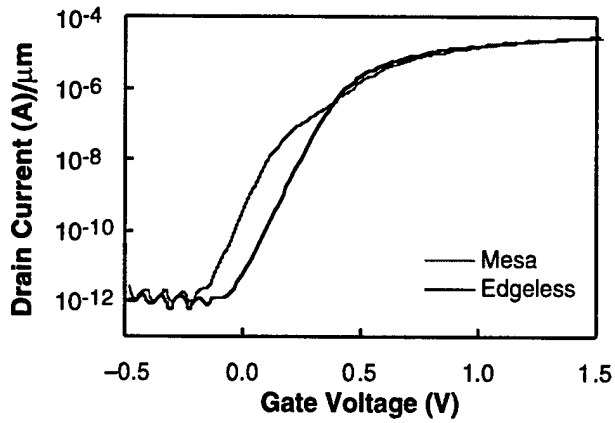

Figure 7-2. Drain current vs gate voltage for mesa-isolated n-FET and edgeless fully depleted SOI transistor. Premature turn-on of the edge of the mesa-isolated n-FET is evident when compared to the turn-on of an edgeless transistor. $L = 0.5\ \mu m$; $W = 8\ \mu m$; $V_{drain} = 0.05\ V$.

75-nm nitride spacers were formed, and the source drains were implanted and activated by rapid thermal annealing. Since the SOI had not been etched into islands, the polysilicon was defined on a planar surface and no antireflective coating was required. Further, active fill was not required to aid CMP, thus eliminating parasitic capacitance between polysilicon gates, metal conductors, and active fill. After deposition and planarization of a 500-nm low-temperature oxide (LTO), contacts were etched and filled with tungsten. Aluminum-silicon was deposited and defined to complete this stage of fabrication. Note that at this point the transistors were not isolated. Then the SOI wafers and oxidized bulk silicon wafers were coated with a layer of LTO deposited by liquid-phase chemical vapor deposition (LPCVD) at a temperature of 430°C. CMP was used to planarize and smooth the surfaces to a roughness of <0.4 nm. The post-CMP film thickness was ~0.5 μm. Then the wafers were immersed in H_2O_2 at 80°C for 10 min to remove any organic contaminants and to activate the surfaces, rinsed, and spun dry in room air.

Each SOI wafer was inverted, bonded to an oxidized bulk silicon wafer, and then transferred to a hot plate for a 300°C 8-h thermal cycle. The handle silicon of the SOI wafer was removed by a wet chemical etch that is selective to the buried oxide. Isolation of the transistors was achieved by defining the active area and etching the buried oxide and SOI. The buried oxide was etched in a CF_4/CHF_3 plasma with a 20:1 minimum selectivity to silicon, and the SOI was etched in a $Cl_2/HBr/O_2$ plasma with a minimum selectivity to oxide of 23:1. Following resist strip, the wafers were treated for 10 min in a piranha solution at 110°C and for 10 min in a peroxide solution at 80°C. The latter two steps were used to smooth the etched sidewalls and chemically grow a 15-nm oxide on the sidewalls [3]. A 50-nm TEOS oxide was then plasma deposited to protect the sidewalls during subsequent processing. After a masked etch of the LTO to expose the underside of the metal probe pads, the wafers were annealed at 400°C for 40 min in a 10:1

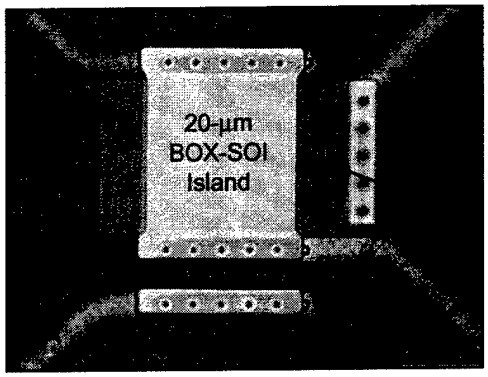

Figure 7-3. Optical micrograph of underside of planar transistor after wafer bonding, active definition of the BOX and SOI, and probe pad etch. The probe pads are outside the field of view. Two tungsten plugs are exposed because of misalignment of active to polysilicon. The lower metal electrode was included for partially depleted device fabrication.

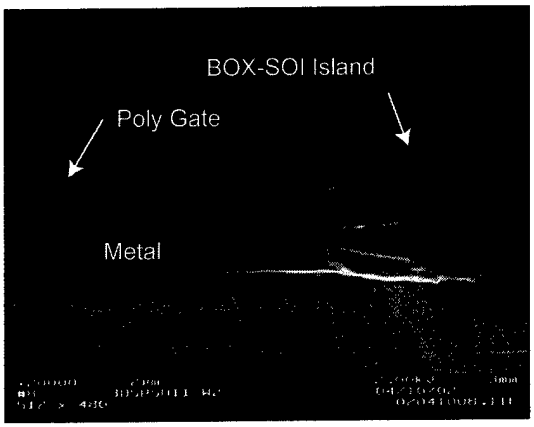

Figure 7-4. Cross section through transistor after isolation, showing the polysilion gate and the SOI and BOX stack. The sample was decorated to show the oxide-oxide bond.

N_2H_2 atmosphere. A photomicrograph of an isolated transistor is shown in Figure 7-3, and a cross-sectional scanning electron micrograph of a similar transistor is shown in Figure 7-4. The utilization of an existing active mask resulted in an active-to-polysilicon alignment error of 2 μm. As a result the minimum width of functionally aligned transistors was 20 μm. In practice, an active mask would be generated by mirroring the existing design data so that the misalignment of active to polysilicon would be a maximum of ±50 nm.

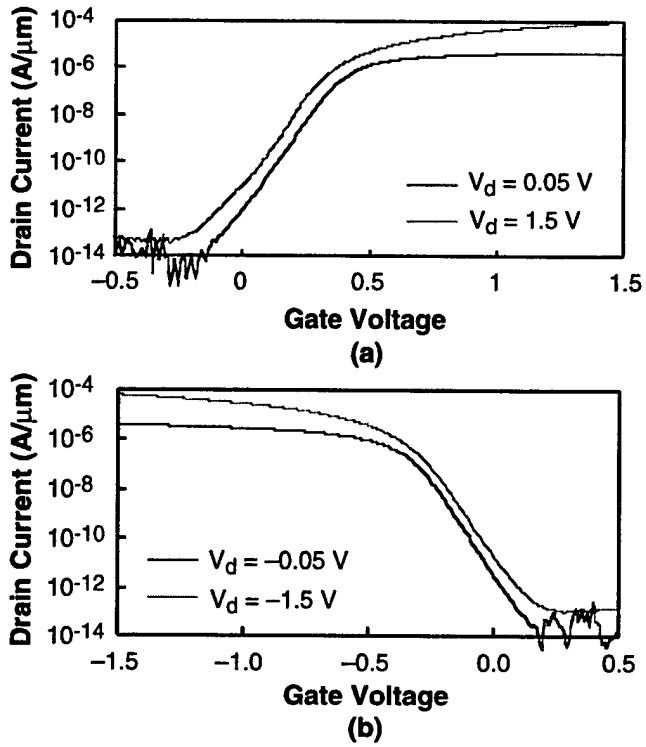

Figure 7-5. Transfer characteristics of planar (a) n-FET and (b) p-FET after isolation, passivation, and anneal. These devices received a second anneal of 20 min at 455°C. L = 0.05 μm; W = 20 μm.

The dc properties of *n*- and *p*-FETs were determined using an HP4156. Typical current-voltage curves are shown in Figure 7-5. These data indicate that the devices do not exhibit parasitic edge conduction. The subthreshold swings of both transistors, 65 mV/decade, are characteristic of a fully depleted technology. A second anneal of 20 min at 455°C was required to improve the sidewall passivation and resulted in a reduction of the off-state leakage of 200% and 45% for the *n*- and *p*-FETs, respectively. There was no evidence of enhanced gate oxide leakage in any of the transistors tested. These results indicate that, by using the low-temperature oxide-oxide bond process, SOI devices can be isolated by an inherently planar technique that simplifies gate lithography and reduces field enhancement at island edges without the complexities of an STI process.

J. Burns
C. Costa
K. Warner

REFERENCES

1. S. K. H. Fung, M. Chan, and P. K. Ko, *IEEE Trans. Electron Devices* **45**, 1105 (1998).

2. K. Warner, W. Mowers, J. A. Burns, D. Lennon, C. L. Keast, D. R. Yost, A. Looomis, and R. Kunz, *2002 IEEE International SOI Conference Proceedings* (IEEE, Piscataway, NJ, 2002), p. 123.

3. C. Paillet, J. P. Joly, F. Tardif, K. Barla, P. Patruno, and D. Levy, *Electrochemical Society Proceedings,* Vol. 95-20 (Electrochemical Society, Pennington, NJ, 1996), p. 366.

REPORT DOCUMENTATION PAGE

Form Approved
OMB No. 0704-0188

Public reporting burden for this collection of information is estimated to average 1 hour per response, including the time for reviewing instructions, searching existing data sources, gathering and maintaining the data needed, and completing and reviewing the collection of information. Send comments regarding this burden estimate or any other aspect of this collection of information, including suggestions for reducing this burden, to Washington Headquarters Services, Directorate for Information Operations and Reports, 1215 Jefferson Davis Highway, Suite 1204, Arlington, VA 22202-4302, and to the Office of Management and Budget, Paperwork Reduction Project (0704-0188), Washington, DC 20503.

1. AGENCY USE ONLY (*Leave blank*)	2. REPORT DATE 15 February 2003	3. REPORT TYPE AND DATES COVERED Quarterly Technical Report, 1 November 2002 – 31 January 2003

4. TITLE AND SUBTITLE

Solid State Research

5. FUNDING NUMBERS

C — F19628-00-C-0002

6. AUTHOR(S)

David C. Shaver

7. PERFORMING ORGANIZATION NAME(S) AND ADDRESS(ES)

Lincoln Laboratory, MIT
244 Wood Street
Lexington, MA 02420-9108

8. PERFORMING ORGANIZATION REPORT NUMBER

2003:1

9. SPONSORING/MONITORING AGENCY NAME(S) AND ADDRESS(ES)

HQ Air Force Materiel Command
AFMC/STSC
Wright-Patterson AFB, OH 45433-5001

10. SPONSORING/MONITORING AGENCY REPORT NUMBER

ESC-TR-2002-089

11. SUPPLEMENTARY NOTES

None

12a. DISTRIBUTION/AVAILABILITY STATEMENT

Approved for public release; distribution is unlimited.

12b. DISTRIBUTION CODE

13. ABSTRACT (*Maximum 200 words*)

This report covers in detail the research work of the Solid State Division at Lincoln Laboratory for the period 1 November 2002–31 January 2003. The topics covered are Quantum Electronics, Electro-optical Materials and Devices, Submicrometer Technology, Biosensor and Molecular Technologies, Advanced Imaging Technology, Analog Device Technology, and Advanced Silicon Technology. Funding is provided by several DoD organizations—including the Air Force, Army, DARPA, MDA, Navy, NSA, and OSD—and also by the DOE, NASA, and NIST.

14. SUBJECT TERMS

quantum electronics
electro-optical devices
materials research
submicrometer technology
biosensor technology
molecular technology
advanced imaging technology
analog device technology
microchip lasers
monolithic detector array
advanced lithography
biofuel cell
focal plane arrays
quantum computing
silicon-on-insulator devices

15. NUMBER OF PAGES
71

16. PRICE CODE

17. SECURITY CLASSIFICATION OF REPORT	18. SECURITY CLASSIFICATION OF THIS PAGE	19. SECURITY CLASSIFICATION OF ABSTRACT	20. LIMITATION OF ABSTRACT
Unclassified	Same as Report	Same as Report	Same as Report